Aluminium microelectromechanical resonator as a probe of superfluid helium

Timo Kamppinen

School of Science

Thesis submitted for examination for the degree of Master of Science in Technology.

Espoo 12.10.2017

Thesis supervisor:

Professor Pertti Hakonen

Thesis advisor:

Docent Vladimir Eltsov

Aalto University
School of Science

AALTO UNIVERSITY
SCHOOL OF SCIENCE

ABSTRACT OF THE
MASTER'S THESIS

Author: Timo Kamppinen

Title: Aluminium microelectromechanical resonator as a probe of superfluid helium

Date: 12.10.2017 Language: English Number of pages: 6+50

Department of Applied Physics

Professorship: Physics of Advanced Materials

Supervisor: Professor Pertti Hakonen

Advisor: Docent Vladimir Eltsov

In this work, the response of magnetomotively driven MEMS resonators have been measured at low temperatures in vacuum (16 mK – 4 K) and superfluid ^{4}He (18 mK – 1 K). The goal post shaped devices (dimensions $\sim 10\,\mu$m) are made from suspended aluminium beams with rectangular cross section $0.15\,\mu\text{m} \times 1\,\mu$m and their operation frequencies range from 300 kHz to 500 kHz. We believe that the force resolution $\Delta F \sim 1$ fN of the devices is sufficient for studying dynamics of a single vortex pinned to the device. In vacuum, the dissipation follows a power law $\Delta f \propto T^{0.4}$ and the resonance frequency increases logarithmically with temperature. The behaviour is attributed to tunneling two level systems present in the structure. In superfluid ^{4}He, the dissipation increases further as a consequence of momentum transfer in collisions with ballistic phonons $\Delta f \propto T^4$ and rotons $\Delta f \propto \exp(-\Delta/T)$. At large oscillation amplitudes, the devices show nonlinear Duffing-like behaviour with an amplitude dependent quadratic frequency shift $f_r = f_0 + \beta x_0^2$, where $\beta < 0$. In superfluid ^{4}He at $T = 18$ mK we observe a collapse of the oscillations at $v_c = 0.17$ m/s independently of the driving force. We interpret this as a sudden increase of the drag force, when the critical velocity for the emission of vortex rings is exceeded.

Keywords: low temperature, superfluid, helium, ^{4}He, MEMS, nonlinear oscillator, Duffing oscillator, dissipation, drag, damping, tunneling, two level system, phonon, roton, quantum vortex, vortex ring

AALTO-YLIOPISTO
PERUSTIETEIDEN KORKEAKOULU

DIPLOMITYÖN
TIIVISTELMÄ

Tekijä: Timo Kamppinen

Työn nimi: Alumiininen mikroelektromekaaninen värähtelijä supraneste heliumin tutkimuksessa

Päivämäärä: 12.10.2017 Kieli: Englanti Sivumäärä: 6+50

Teknillisen fysiikan laitos

Professuuri: Kehittyneiden materiaalien fysiikka

Työn valvoja: Professori Pertti Hakonen

Työn ohjaaja: Dosentti Vladimir Eltsov

Tässä työssä mitattiin mikroelektromekaanisten värähtelijöiden vastetta magneetti- ja sähkökenttien synnyttämään herätteeseen kylmissä lämpötiloissa sekä tyhjiössä (16 mK – 4 K) että supraneste heliumissa (^{4}He, 18 mK – 1 K). Kyseisten laitteiden koko on luokkaa 10 µm, ja ne on valmistettu alumiinista jalkapallomaalin muotoon (kaksi jalkaa ja puomi). Maali muodostuu palkeista, joiden poikkipinta on neliskulmainen ja kooltaan 0.15 µm × 1 µm. Värähtelijöiden ominaistaajuudet sijaitsevat välillä 300 kHz – 500 kHz. Uskomme että laitteiden osoittama voimien erottelukyky $\Delta F \sim 1$ fN on riittävän tarkka yksittäisten kvanttipyörteiden dynamiikan tutkimiseen. Tyhjiössä resonaattoreiden häviöt seuraavat potenssilakia $\Delta f \propto T^{0.4}$ ja ominaistaajuudet kasvavat logaritmisesti lämpötilan noustessa. Kyseinen käyttäytyminen liittyy tunneloituviin kaksitasosysteemeihin laitteiden rakenteissa. Supraneste heliumissa häviöt kasvavat lisää, sillä resonaattorit törmäilevät ballistisesti eteneviin fononeihin $\Delta f \propto T^4$ ja rotoneihin $\Delta f \propto \exp(-\Delta/T)$ siirtäen liikemääräänsä niille. Suurilla värähtelyamplitudeilla laitteet käyttäytyvät epälineaarisesti Duffing-resonaattorin kaltaisesti, ja resonanssitaajuus siirtyy neliöllisesti amplitudin kasvaessa $f_r = f_0 + \beta x_0^2$, jossa $\beta < 0$. Supraneste heliumissa, 18 mK lämpötilassa, havaitaan värähtelyiden yhtäkkinen pysähtyminen kun saavutetaan nopeus $v_c = 0.17$ m/s riippumatta herätteen voimakkuudesta. Tulkitsemme tämän äkillisenä häviöiden kasvuna, kun kriittinen nopeus pyörrerenkaiden emissiolle ylitetään.

Avainsanat: matalat lämpötilat, supraneste, helium, ^{4}He, MEMS, Duffing oskillaattori, häviöt, väliaineen vastus, tunneloituminen, kaksitasosysteemi, fononi, rotoni, kvanttipyörre, pyörrerengas

Contents

Symbols and abbreviations

Symbols

κ	quantum of circulation
k_B	Boltzmann constant
$h, \hbar$	Planck, reduced Planck constant
θ_D	Debye temperature
T	temperature
p	pressure
ρ	density
H	feet length
L	beam length
w	beam/leg width
d	beam/leg thickness
k	spring constant
E	elastic modulus
m_0	effective mass
$\tilde{m}$	added mass
$\omega_0 = 2\pi f_0$	linear resonance frequency
$\gamma = 2\pi\Delta f$	drag coefficient
$Q = \omega_0/\gamma$	quality factor
Q^{-1}	loss factor
$\delta\omega_0 = 2\pi\delta f_0$	frequency shift
$\mathbf{B}$	magnetic field
x	displacement
$\dot{x}$	velocity
$\ddot{x}$	acceleration
x_0	oscillation amplitude
x_c	critical oscillation amplitude
$x_{\max}$	displacement amplitude in resonance
t	time
x^s	out-of-phase displacement
x^c	in-phase displacement
k_i	nonlinear elastic coefficient
m_i	nonlinear mass coefficient
Γ_i, γ_i	nonlinear damping coefficients
k_i'	general nonlinear coefficients
$\omega_r = 2\pi f_r$	nonlinear resonance frequency
β	Duffing parameter
σ	scattering cross section
c	velocity of sound
k_0	roton wave number
Δ_{rot}	roton gap
P_0	density of states
$\tau_{\min}$	minimum relaxation time
γ_c	electron-TLS coupling constant
α_L	linear thermal expansion coefficient
C	heat capacity

Abbreviations

^{3}He	helium 3
^{4}He	helium 4
LHe	liquid helium
He I	liquid helium
He II	superfluid helium
AC	alternating current
DC	direct current
MEMS	microelectromechanical system
NEMS	nanoelectromechanical system
TED	thermoelastic damping
TLS	two-level system
STM	standard tunneling model
SEM	scanning electron microscope
RRR	residual resistivity ratio
Al	aluminium
Si	silicon
SiO_2	silicon oxide

Chapter 1

Introduction

The most common isotope of helium, ^{4}He, also known as the light gas used to fill balloons, has the most interesting properties when cooled to temperatures near the absolute zero, where quantum phenomena become important. As a result of the weak attraction between the (noble and light) helium atoms, the boiling point of the substance is rather low at 4.2 K temperature in atmospheric pressure. Due to the large zero-point energy of ^{4}He, it remains a liquid down to the absolute zero temperature under conventional pressures ($p < 25$ bar). However, near 2.2 K a different kind of phase transition occurs. At this so called lambda transition, a fraction of the fluid becomes superfluid, which has zero viscosity and zero entropy. To distinguish between the two different states, the classical fluid above the transition temperature is called helium I (He I), and the quantum fluid below the transition temperature is called helium II (He II). The quantum fluid has normal (classical) fluid and superfluid components, and the fraction of the superfluid increases with lowering temperature from all-normal fluid at the lambda transition to all-superfluid at zero temperature. As a result of the zero viscosity, the superfluid can flow through narrow channels without friction, much like electrons can flow without resistance in superconductors.

One important property of superfluids is the existence of quantized vortices, which are characterized by the quantum of circulation $\kappa = h/M$, where h is the Planck constant and M is the mass of the atom. Near the absolute zero temperature, the energy dissipated by a quantized vortex is extremely small and such a vortex line can persist practically forever. Helical distortions along a vortex line are called Kelvin waves (KW). Quantum turbulence consists of a chaotic tangle of vortex lines. Its relaxation involves energy cascades of different nature, vortex reconnections and microscopic dissipation mechanisms. Cascade of Kelvin waves towards lower wavelengths is believed to have an important role in the relaxation at $T \to 0$ limit in the absence of normal fluid [1]. However, conclusive experimental proof of the Kelvin wave cascade on a single vortex has not been achieved yet.

Oscillating objects, such as tuning forks, wires, grids and spheres, have proven to be useful probes of temperature, pressure and viscosity in the superfluids ^{4}He and

^{3}He. They have also been used as generators and detectors of turbulence, cavitation and sound (first and second) in the fluids [2, 3, 4, 5]. The properties of the fluids are usually determined from measured changes in mechanical resonance response due to the forces experienced by the oscillator moving through the fluid. Microelectromechanical (MEMS) and nanoelectromechanical systems (NEMS) have recently emerged as promising new tools for exploring the quantum fluids [6, 7, 8, 9, 10, 11]. Their advantages over the larger devices include higher sensitivity to forces, lower power dissipation, and the possibility to probe the fluids on scales much smaller than the intervortex distance and even smaller than the coherence length (in ^{3}He). Our goal is to fabricate an oscillator with a high force sensitivity and a trapping site for a single quantized vortex line, and to measure the dissipative and reactive forces that this vortex exerts on the device, which is driven resonantly. A low spring constant (or in other words, low mass and frequency) and high Q-value are needed for high force sensitivity. Furthermore, small dimensions are required to prevent undesirable pinning of other vortices to the device, which would obviously prevent measurements on a single vortex. In pursuit of this goal, we have fabricated magnetomotively driven MEMS resonators with dimensions $\sim 10\,\mu$m made from suspended aluminium beams with cross section $0.15\,\mu\text{m} \times 1\,\mu$m, spring constant $k \sim 0.1\,\text{N}\,\text{m}^{-1}$, effective mass $m_0 \sim 10\,$pg and frequencies in the range from 300 kHz to 500 kHz.

In this work, we present the response of our MEMS devices measured at low temperatures in vacuum (16 mK – 4 K) and supefluid ^{4}He (18 mK – 1 K). The intrinsic width has a power-law dependence on temperature below 1 K with a transition to a rather flat region above 1 K. The behaviour is accompanied by a logarithmic frequency shift with increasing temperature, which shows a maxima around 1 K. Interestingly, quantum mechanical effects play a key role in the observed behaviour. The damping can be explained in the framework of two-level systems, whose dynamics is governed by quantum tunneling. The single-material structure of our devices is ideal for studying the internal losses occurring in polycrystalline metals at low temperatures.

At $T < 1\,$K, the drag force in superfluid ^{4}He is due to momentum transfer with ballistic phonons $\Delta f \propto T^4$ and rotons $\Delta f \propto \exp(-\Delta/T)$. The temperature dependent intrinsic width and ballistic drag enable thermometry with these devices directly in the superfluid at milliKelvin temperatures. At large oscillation amplitudes, the response of the devices become nonlinear and show Duffing-like behaviour, where the resonance frequency is shifted towards lower frequencies quadratically with the oscillation amplitude $f_r = f_0 + \beta x_0^2$ (with $\beta < 0$). The value of β is independent of temperature at $T < 2\,$K. However, β becomes more negative in the superfluid ^{4}He, possibly due to nonlinear mass enhancement. Similar behaviour has been reported in [10], where the measurements were conducted in ^{3}He. In superfluid ^{4}He at $T = 18\,$mK we observe a collapse of the oscillations at velocity $v_c = 0.17\,$m/s independently of the driving force. We interpret this as a sudden increase of the drag force when the critical velocity for the emission of vortex rings is exceeded.

First succesfull measurement of bulk superfluid ^{4}He properties conducted with a nanomechanical resonator (with beam cross section $100\,\mathrm{nm} \times 100\,\mathrm{nm}$) at $T > 1\,\mathrm{K}$ was reported only very recently by Bradley et al. in [11]. Note that the thickness of our aluminium beams lies in the nanometer scale ($d = 150\,\mathrm{nm}$) and in this sense our measurement is also one of the first to be succesfully conducted in bulk superfluid and the first in the milliKelvin temperature range.

Chapter 2

Theoretical background

This chapter starts by introducing the magnetomotive drive and detection method of the devices. The device shape, and the corresponding resonance properties are also discussed. Next, the equation of motion in the linear and nonlinear regime are discussed. The expected force sensitivity is estimated here as well. Finally, the vast variety of damping mechanisms affecting these devices are discussed.

2.1 Magnetomotive drive and detection

The geometry of the MEMS oscillators comprises of two cantilever feet connected by a paddle, as shown in Fig. 2.1. The feet and the paddle have rectangular cross section $d \times w = 0.15\,\mu\text{m} \times 1.0\,\mu\text{m}$ and dimensions $H, L \sim 10\,\mu\text{m}$. The fundamental resonance mode of the devices corresponds to out-of-plane and in-phase oscillation of the two cantilever feet connected by the (rigid) paddle. The dynamic mode shape is well approximated by the static mode shape obtained by applying a constant load at the end of the cantilever feet [7, 12]. Thus, the effective spring constant of our devices is that of the two parallel rectangular cantilever feet

$$k = \frac{Ewd^3}{2H^3}, \tag{2.1}$$

where E is the elastic modulus of the material, w is the width, d is the thickness and H is the length of a leg. The effective mass of one cantilever foot is $m_{\text{foot}} = 33/140\rho dwH$, where ρ is material density. The rigid paddle (length L) at the end of the feet acts as a simple mass load ($m_{\text{paddle}} = \rho dwL$). Thus, the total effective mass is

$$m_0 = 2m_{\text{foot}} + m_{\text{paddle}} = \rho dw\left(\frac{33}{70}H + L\right). \tag{2.2}$$

The mechanical resonance frequency is then given by

$$\omega_0 = 2\pi f_0 = \sqrt{\frac{k}{m_0}} = \sqrt{\frac{E}{\rho}\frac{d^2}{(33/35)H^4 + 2H^3L}}. \tag{2.3}$$

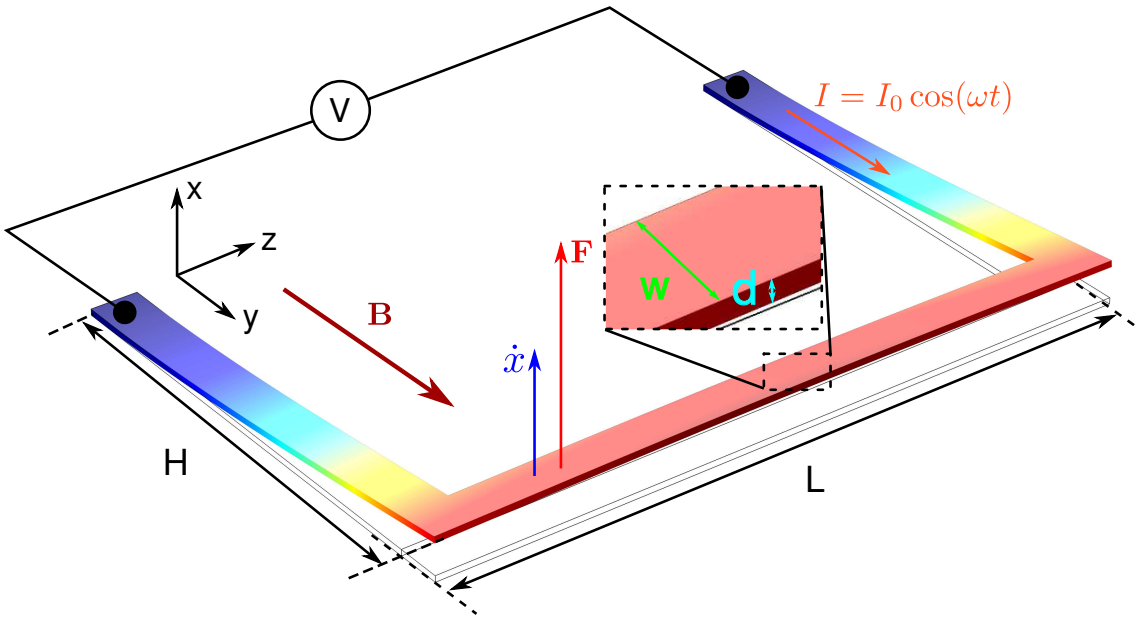

Figure 2.1: Dynamical mode shape of the fundamental mode, based on Comsol simulation (structural mechanics toolbox). The magnetomotive drive and detection scheme, geometrical parameters and the coordinate system used in this work are also depicted.

For a reference to the spring constant, effective mass and resonance frequency, see e.g. [13] or any other textbook in the field of mechanical engineering.

It is well known that the properties of microfabricated materials often differ greatly from those of the corresponding bulk materials. Many fabrication methods and conditions can lead to drastically different charasteristics of the materials. As such, universal material properties applicable to all devices in the nano- and microscales do not exist. However, the measured and simulated resonance frequency of our devices typically agree within 5%, when the bulk properties of aluminium are used [12]. Thus, the elastic modulus $E = 70\,\mathrm{GPa}$ and the density $\rho = 2700\,\mathrm{kg/m^3}$ of bulk aluminium are assumed. For the typical device dimensions ($d \times w = 0.15\,\mu\mathrm{m} \times 1.0\,\mu\mathrm{m}$, $H, L \sim 10\,\mu\mathrm{m}$), we obtain $k \sim 0.1\,\mathrm{N/m}$ and $m_0 \sim 10\,\mathrm{pg}$.

The measurements in this work are done using the fundamental mode, which is easy to excite and detect with a magnetomotive method. When the MEMS device is placed in a constant magnetic field $\mathbf{B} = B\hat{\mathbf{y}}$ and an AC excitation current $I = I_0 \cos(\omega t)$ is fed through the device, the paddle experiences a Lorentz force

$$\mathbf{F}(t) = I(t)[-L\hat{\mathbf{z}} \times B\hat{\mathbf{y}}] = I_0 LB \cos(\omega t)\hat{\mathbf{x}}, \tag{2.4}$$

where $\hat{\mathbf{x}}$, $\hat{\mathbf{y}}$ and $\hat{\mathbf{z}}$ are the unit vectors in the corresponding directions (see Fig. 2.1). Ideally, the two feet are exactly parallel to the magnetic field and do not experience the magnetic force. The Lorentz force experienced by the paddle drives the resonator into oscillatory motion at the excitation frequency ω. Due to the proximity to the

silicon surface, our devices are limited to relatively small oscillation amplitudes, so that the motion of the paddle is in practice always perpendicular to the magnetic field even at the highest drives. The motion of the paddle through the magnetic field induces a voltage difference V between the two ends of the beam (Faraday's law of induction)

$$V(t) = LB\dot{x}(t) = LB\omega[x^s \cos(\omega t) - x^c \sin(\omega t)], \tag{2.5}$$

where $\dot{x}$ is the velocity of the paddle and x^s and x^c are the the out-of-phase and in-phase components of the displacement (see the next section).

2.2 Equation of motion

The MEMS devices can be treated as damped oscillators driven by the Lorentz force $F(t) = F_0 \cos(\omega t)$, where $F_0 = I_0 LB$. At sufficiently small oscillation amplitudes, harmonic approximation is valid. Denoting the beam displacement x, velocity $\dot{x}$ and acceleration $\ddot{x}$ and including the damping force $F_d = -m_0\gamma\dot{x}$ and the restoring force $F_i = -m_0\omega_0^2 x$, the equation of motion becomes

$$\ddot{x} + \gamma\dot{x} + \omega_0^2 x = \frac{F_0}{m_0}\cos(\omega t), \tag{2.6}$$

where $\gamma = 2\pi\Delta f$ is the damping coefficient (in units $\mathrm{rad\,s^{-1}}$).

2.2.1 Force sensitivity

In vacuum, the damping is due to the intrinsic losses in the material, while in fluids the damping increases further e.g. due to viscous drag. We can estimate the force resolution to dissipative forces by differentiating F_d with respect to γ:

$$|\Delta F_d| = m_0\dot{x}\Delta\gamma = kx\frac{\Delta Q}{Q^2}, \tag{2.7}$$

where $\Delta\gamma$ is the error estimate of the measured damping coefficient, $Q = \omega_0/\gamma$ is the quality factor and $\Delta Q/Q$ is the relative error estimate for the measured Q-value. Inertial forces cause a change to the resonance frequency, and the sensitivity to inertial forces is given by

$$|\Delta F_i| = 2m_0\omega_0\Delta\omega_0 x \approx kx\frac{\Delta Q}{Q^2}, \tag{2.8}$$

where $\Delta\omega_0$ is the error estimate of the measured resonance frequency. The last approximation is valid, if we assume that the error in resonance frequency and the line width are linked through $\Delta\omega_0 = \frac{1}{2}\Delta\gamma$. For high force sensitivity, a small spring constant, high Q-value, and accurate determination of the Q-value for a given

oscillation amplitude are required. It is evident from Eq. (2.1) that thin ($k \propto wd^3$) and long legs ($k \propto H^{-3}$) are required for a low spring constant. The relative importance of the terms is reflected in the choise of the dimensions $d = 150\,\text{nm}$, $w = 1\,\mu\text{m}$ and $H \sim 10\,\mu\text{m}$. For typical spring constant $k = 0.1\,\text{N}\,\text{m}^{-1}$, oscillation amplitude $x = 10\,\text{nm}$, expected sensitivity $\Delta Q/Q = 0.1$ and $Q = 1 \times 10^4$, the force resolution becomes $|\Delta F_d| \sim |\Delta F_i| \sim 10\,\text{fN}$.

2.2.2 Steady-state solutions

The steady-state solution to Eq. (2.6), established when the excitation has been applied for a sufficiently long time ($\gtrsim 1/\gamma$), is of the form

$$x(t) = x^s(\omega)\sin(\omega t) + x^c(\omega)\cos(\omega t),$$

where x^s and x^c produce the Lorentzian line shapes in the frequency domain:

$$x^s(\omega) = \frac{F_0}{m_0}\frac{\gamma\omega}{(\omega_0^2 - \omega^2)^2 + \gamma^2\omega^2} \tag{2.9}$$

$$x^c(\omega) = \frac{F_0}{m_0}\frac{\omega_0^2 - \omega^2}{(\omega_0^2 - \omega^2)^2 + \gamma^2\omega^2}. \tag{2.10}$$

An example plot of the Lorentzian line shapes can be seen in Fig. 2.2. The maximum oscillation amplitude is obtained at the resonance frequency $\omega_0\sqrt{1 - 1/2Q^2} \approx \omega_0$, where the last approximation is valid when $Q \gg 1$. At resonance, the in-phase component of the displacement x^c is zero, and the maximum displacement amplitude is given by the out-of-phase component

$$x_{\text{max}} = x^s(\omega_0) = \frac{F_0}{m_0}\frac{1}{\gamma\omega_0} = \frac{F_0}{k}Q. \tag{2.11}$$

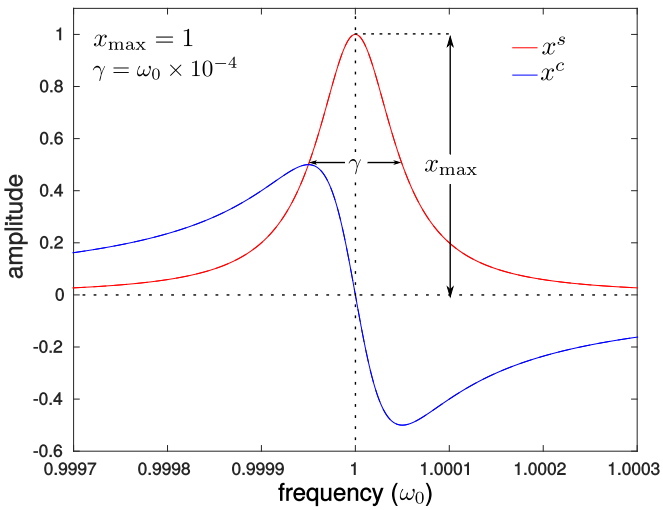

Figure 2.2: An example plot of the linear resonance response described by Eqs. (2.9) and (2.10), when $Q = 1 \times 10^4$.

The full width at half height (line width) of the resonance peak drawn by the out-of-phase component x^s is given by the damping coefficient γ.

2.2.3 Nonlinear resonance response

At large oscillation amplitudes, intrinsic nonlinearities in spring constant, mass and dissipation can arise, where the properties become functions of the displacement amplitude. Three types of nonlinearity exist:

- Material nonlinearity, when material is used beyond it's elastic limit, or it displays non-linear friction.
- Nonlinearities arising from the used drive and/or detection scheme.
- Geometrical nonlinearity, arising from change in geometry, when device shape changes at large oscillation amplitudes.

The yield stress of the thin Al structure is not exactly known. However, the data presented in [14] indicate that the yield stress in $\sim 100\,\mathrm{nm}$ thick Al films is greater than 300 MPa. The highest stress in the structures occurs at the fixed end of the legs, and is given by [13]

$$\sigma_{\max} = \frac{3Ed}{2H^2} x_{\max}. \tag{2.12}$$

For typical devices with feet length $H = 10\,\mu\mathrm{m}$ and maximum oscillation amplitude $x_{\max} = 100\,\mathrm{nm}$, the maximum stress is approximately 16 MPa which is an order of magnitude smaller than the expected yield stress. Thus, the Al in our structures is within the elastic limit. On the other hand, nonlinear friction cannot really be excluded without measurement.

The driving force in the magnetomotive method is independent of the displacement amplitude in a homogenous magnetic field. However, the direction of the velocity of the paddle changes slightly as a function of the displacement, as the feet of the structure bend. This could cause a nonlinear decrease in the generated voltage, which depends only on the x-component of the velocity. Our devices are limited to such small oscillation amplitudes (due to proximity to the silicon substrate) that this effect is negligible. Thus, nonlinearities arising from the used drive and detection scheme can be neglected.

We are left with the geometrical nonlinearity, of which a good analytical description is given by Collin et al. in [15]. Expanding to the third order, the nonlinear equation of motion can be written as

$$\begin{aligned} m_0(1 + m_1 x + m_2 x^2)\ddot{x} + (\Gamma_0 + \Gamma_1 x)\,\dot{x}^2 + m_0\gamma(1 + \gamma_1 x + \gamma_2 x^2)\dot{x} \\ + k(1 + k_1 x + k_2 x^2)x = F_0 \cos(\omega t), \end{aligned} \tag{2.13}$$

where m_i are the nonlinear mass coefficients, γ_i and Γ_i are the nonlinear damping coefficients and k_i are the nonlinear spring constants. In general, a nonlinear reactive

contribution (linked to the intrinsic damping through the Kramers-Kronig relations) should also be considered, but since it has the same role in the equation as the nonlinear mass, we have not written it out explicitly (instead, it is included in the nonlinear mass). For a given mode shape, the nonlinear parameters can be evaluated with the analytical expressions given in [15].

In practice, the geometrical nonlinear damping is small and we have not observed it experimentally. For narrow frequency sweeps (high Q) the motion of the device is captured by the solution of the simplified expression

$$\ddot{x} + \gamma\dot{x} + \omega_0^2(1 + k_1'x + k_2'x^2)x = \frac{F_0}{m_0}\cos(\omega t), \tag{2.14}$$

where all nonlinear effects are included in the nonlinear constants k_1' and k_2' (see reasoning at the end of this subsection). The solution is a sum of oscillating terms

$$\sum_{n=0}^{\infty} x_n^s \sin(n\omega t) + x_n^c \cos(n\omega t). \tag{2.15}$$

Seeking solution only for the first harmonic ($n = 1$) results in modified Lorentzian functions

$$x_1^s(\omega) = \frac{F_0}{m_0}\frac{\gamma\omega}{(\omega_r^2 - \omega^2)^2 + \gamma^2\omega^2} \tag{2.16}$$

and

$$x_1^c(\omega) = \frac{F_0}{m_0}\frac{\omega_r^2 - \omega^2}{(\omega_r^2 - \omega^2)^2 + \gamma^2\omega^2}, \tag{2.17}$$

where the resonance position ω_r is a function of the displacement amplitude:

$$\omega_r = \sqrt{\omega_0^2 + 2\omega_0\beta x_0^2} \approx \omega_0 + \beta x_0^2, \tag{2.18}$$

and

$$\beta = \omega_0\left(\frac{3}{8}k_2' - \frac{5}{12}k_1'^2\right).$$

The amplitude $x_0 = \sqrt{(x_1^s)^2 + (x_1^c)^2}$ is found by solving the roots of the polynomial equation

$$-\left(\frac{F_0}{m_0}\right)^2 + [\gamma^2\omega^2 + (\omega^2 - \omega_0^2)^2]x_0^2 - 4\beta\omega_0(\omega^2 - \omega_0^2)x_0^4 + 4\beta^2\omega_0^2x_0^6 = 0, \tag{2.19}$$

which is cubic in terms of x_0^2. Thus, there exists three roots for x_0^2, which can be found analytically. The number of physical (real and positive) solutions depends on the oscillation amplitude. Below the threshold amplitude

$$x_c = \frac{2}{3^{3/4}}\sqrt{\frac{\gamma}{|\beta|}}, \tag{2.20}$$

only one of the roots is physical. At larger oscillation amplitudes $x_{\max} > x_c$, three branches coexist, of which two are stable and one is unstable. The response of the de-

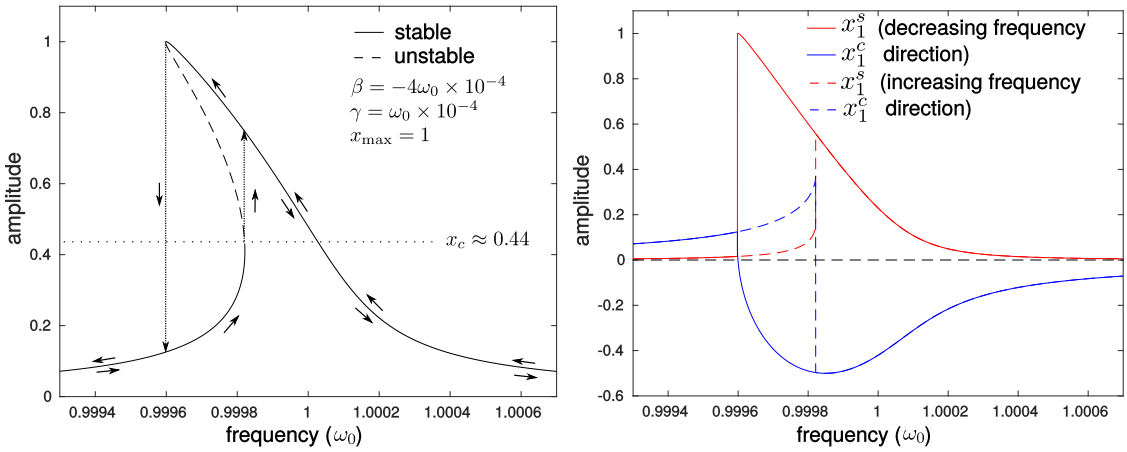

Figure 2.3: (left:) An example plot of the oscillation amplitudes obtained from Eq. (2.19), when the maximum amplitude $x_{\max}$ is larger than the threshold amplitude x_c. The resonance frequency shifts towards lower frequencies with increasing oscillation amplitude, since β is negative. The solution is bistable between the two dotted arrows and the actual response depends on the initial conditions (frequency sweep direction) as indicated by the arrows. (right:) The modified Lorentzian curves obtained from Eqs. (2.16) and (2.17) with the same parameters as in the figure on the left. Note that the unstable solution is not depicted in this figure, but the red and blue dashed lines correspond to the response in the increasing frequency direction.

vice then depends on the direction of the frequency sweep, as shown in Fig. 2.3.

When $x_{\max} > x_c$, the highest amplitude is obtained when sweeping frequency in the direction of the nonlinear coefficient β (i.e. downwards for negative β) and in the high-Q limit the maximum amplitude is obtained at the nonlinear resonance frequency $\omega_{\text{res}} = \omega_r(x_{\max})$. The maximum amplitude depends on the excitation force and is given by the out of phase component

$$x_{\max} = x_1^s(\omega_{\text{res}}) = \frac{F_0}{m_0}\frac{1}{\gamma\omega_{\text{res}}} = \frac{\omega_0}{\omega_{\text{res}}}\frac{F_0}{k}Q, \tag{2.21}$$

which differs from the linear expression Eq. (2.11) only by the prefactor $\omega_0/\omega_{\text{res}}$, arising from the change in the spring constant. The frequency shifts are always smaller than 1% of the resonance frequency, and the prefactor is practically one. Note that the in-phase component x_1^c is zero at resonance as in the linear case. The linear resonance frequency ω_0 and damping coefficient γ can not be determined directly from the measured resonance position and line width as in the linear regime, but they are acquired (together with the nonlinear parameter β) from fits to Eqs. (2.16) and (2.17).

When $x_{\max} > x_c$ and the frequency is swept in the direction opposite to the nonlinear coefficient (i.e. upwards for negative β), the excitation frequency never actually reaches frequency ω_r and the resonance condition is not met. Far from the linear resonance frequency ω_0, oscillation amplitude is small and ω_r resides close to ω_0.

When the excitation frequency approaches ω_0, the oscillation amplitude increases and ω_r approaches the excitation frequency ω. However, before the excitation frequency and ω_r actually meet, a jump from the lower stable branch to the higher stable branch occurs and ω_r shifts past the excitation frequency.

Neglecting the nonlinear damping terms, the solution to the full nonlinear Eq. (2.13) is the same as for the simplified Eq. (2.14), apart from the term β, which becomes a function of all the nonlinear parameters and frequency [15]. However, for sufficiently narrow sweeps (high Q), the parameter β can be taken as a constant. To take into account nonlinear damping, such as turbulent drag ($\propto \dot{x}^2$), the solution to Eq. (2.13) should be used. In this case the damping coefficient γ in Eqs. (2.16) and (2.17) is replaced with a nonlinear damping coefficient $\gamma_{\mathrm{nonlin}} = \gamma + \beta_\gamma x_0^2$. The change is reflected also in the polynomial equation for solving x_0, which becomes

$$-\left(\frac{F_0}{m_0}\right)^2 + [\gamma^2\omega^2 + (\omega^2 - \omega_0^2)^2]x_0^2 + [2\beta_\gamma\gamma\omega^2 - 4\beta\omega_0(\omega^2 - \omega_0^2)]x_0^4 + [\beta_\gamma^2\omega^2 + 4\beta^2\omega_0^2]x_0^6 = 0. \quad (2.22)$$

2.2.4 Finite element analysis of the geometrical nonlinearity

To estimate the effect of the geometrical nonlinearity in our devices, finite element analysis for sample 5NF with dimensions $L = 14.7\,\mu\mathrm{m}$, $H = 13.0\,\mu\mathrm{m}$ and cross section $d \times w = 0.15\,\mu\mathrm{m} \times 1.11\,\mu\mathrm{m}$ has been done. We use Comsol multiphysics program, and the model of the resonator consists of 1.6×10^4 elements. The mesh is optimised with adaptive mesh refinement which is applied in an initial eigenfrequency analysis. An artificial damping (isotropic structural loss factor 5×10^{-5}) is applied to the material, which results in a Q-value of 2×10^4. The response of the driven device is obtained from a frequency domain study, which uses MUMPS (a MUltifrontal Massively Parallel sparse direct Solver) and Newton's method to obtain the steady state solution at each frequency (parametric sweep).

When geometrical nonlinearity is enabled in the study, the line shapes shown in Fig. 2.4 (middle panel) are produced. The simulations indicate a negative shift of the resonance frequency (left panel) with $\beta = -9.8 \times 10^{-4}\,\mathrm{Hz/nm^2}$. At small amplitudes, the line width is practically constant (inset) and the displacement is directly proportional to the excitation force (right panel). At high oscillation amplitudes ($\gtrsim 50\,\mathrm{nm}$), deviations from the expected Duffing-like behaviour occur and the quadratic fits to the frequency shift (left panel) and line width (inset) do not present the data well. This might indicate limitations of the Duffing model at high amplitudes. For example, the higher order modes (n>1) in Eq. (2.15) could become important, or the assumption of constant β breaks down.

At even higher excitation forces, the convergence of the problem becomes poor, likely due to the high gradients in the solution, when the oscillation amplitude approaches

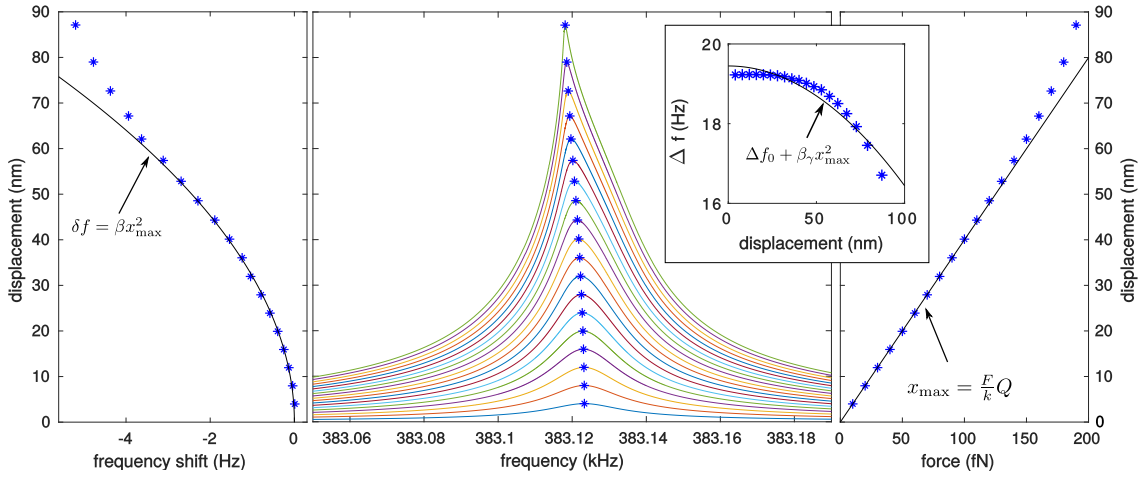

Figure 2.4: (middle:) The frequency response of the sample 5NF at different driving forces based on finite element analysis. The blue asterisks indicate the amplitude and position of the resonance. The Q-value of the device is determined from a Lorentzian fit to the smallest peak (not shown). (left:) Nonlinear shift of the resonance frequency (x-axis) as a function of the displacement amplitude (y-axis) and a quadratic fit to the data at small amplitudes. (right:) The displacement amplitude at resonance as a function of the excitation force. The linear fit to the data at small amplitudes provides the spring constant k of the device. (inset:) The line width of the nonlinear peak as a function of the displacement amplitude and a quadratic fit to the data. The presented line widths are obtained simply from Eq. (2.11), which gives $\Delta f = (F_0 f_0)/(k x_{\max})$.

the critical value x_c. The convergence can be improved by using smaller frequency stepping (since we use the previous solution as an initial guess for the next step) and smaller elements in the mesh. However, these approaches increase the solution time (and RAM requirements) significantly. To keep computation time reasonable (~ 60 h for the highest peak), finer frequency stepping is used near the peak (where gradients are high and convergence is poor) and gradually coarser steps are taken further from the peak.

2.3 Intrinsic damping

The quality factor $Q = \omega_0/\gamma = f_0/\Delta f$ is the ratio of the energy stored in the oscillations to the energy lost per cycle. Higher Q-value indicates lower losses. In practice, we measure damping by determining $\Delta f = \gamma/2\pi$ from fits to the Lorentzian (Eq.(2.9) and (2.10)) or modified Lorentzian (Eq. (2.16) and (2.17)) curves. The damping is directly proportional to the loss factor Q^{-1}, which is often used in the literature. Since the force resolution of a mechanical resonator is limited by the Q-value, understanding of these loss mechanisms is important. We consider here possible sources of damping in our devices. For a more thorough review, see e.g.

[16] and the citations within. To give an idea of the relative importance of the different damping mechanisms, note that the typical quality factors measured for our devices at lowest temperatures are $Q \sim 10^4$ (which corresponds to the loss factor $Q^{-1} \sim 10^{-4}$).

2.3.1 Magnetomotive damping

Before going to the damping occurring actually in the resonators, we consider an external loss mechanism called the magnetomotive damping. The mechanism arises from eddy currents in the external measurement circuit, driven by the magnetomotive force (voltage) generated by the device. The damping increase quadratically with an increasing magnetic field and is inversely proportional to the impedance of the external circuirtry.

The mechanical resonator is electrically equivalent to the parallel combination of a capacitor C_m, an inductor L_m and a resistor R_m. A comparison of the voltage generated over the magnetomotively driven mechanical resonator and the equivalent (unloaded) circuit gives [17]

$$C_m = \frac{m}{L^2B^2}, \quad L_m = \frac{L^2B^2}{\omega_0^2 m} \quad \text{and} \quad R_m = \frac{L^2B^2}{\omega_0 m}Q_0,$$

where ω_0 and Q_0 are the unloaded resonance frequency and quality factor, corresponding to an infinite impedance of the external (open) circuit. An useful quantity is the charasteristic impedance

$$Z_c = \sqrt{\frac{L_m}{C_m}} = \frac{L^2B^2}{\omega_0 m},$$

which is proportional to the square of the magnetic field. When the equivelant circuit is loaded with a finite external load $Z_{\text{ext}} = R_{\text{ext}} + iX_{\text{ext}}$, changes in the apparent resonance frequency and width occur. To first order, the loaded values are [17]

$$f_L = f_0\sqrt{1 + \frac{Z_c X_{\text{ext}}}{|Z_{\text{ext}}|^2}} \tag{2.23}$$

and

$$\frac{1}{Q_L} = \frac{1}{Q_0} + \frac{Z_c R_{\text{ext}}}{|Z_{\text{ext}}|^2}, \tag{2.24}$$

where X_{ext} and R_{ext} are the imaginary and real parts of the external load, respectively. In our setup, the external load consists of the resistance in the excitation ($\sim 1\,\text{k}\Omega$) and detection ($\sim 1\,\text{M}\Omega$) lines connected parallel with the device (see section 3.2). The (large and parallel) resistance of the detection line can be detected. However, the parallel stray capacitance of the wires $C_{\text{stray}} \sim 100\,\text{pF}$ corresponds to $\sim 5\,\text{k}\Omega$ impedance at the typical device frequency ($\sim 300\,\text{kHz}$). The impedance is comparable to the resistance of the excitation line, and cannot be neglected. The magnitude

of the external impedance is $|Z_{\text{ext}}| \approx 1\,\text{k}\Omega$ with $R_{\text{ext}} \sim 1\,\text{k}\Omega$ and $X_{\text{ext}} \sim -0.2\,\text{k}\Omega$. For typical device parameters $L \sim 10\,\mu\text{m}$, $\omega_0 \sim 2\pi \times 300\,\text{kHz}$, $m \sim 10\,\text{pg}$ and magnetic field $B = 83\,\text{mT}$, we get $Z_c \approx 3.7 \times 10^{-5}\,\Omega$. The expected increase in the loss factor is $Q^{-1} \approx 3.7 \times 10^{-8}$ and the expected frequency shift is $\delta f = -1\,\text{mHz}$.

2.3.2 Boundary losses

Boundary losses occur at the interface between the MEMS resonator and the supporting structure. Three mechanisms, namely elastic wave radiation, viscoelasticity and microsliding are considered here.

Elastic wave radiation to the support arises when the resonator applies time-harmonic forces and moments at the clamped end of the feet. Consequently, the mechanical energy of the oscillator is radiated to the support where it eventually dissipates (assuming that the radiated energy does not reflect back into the resonator). Cross and Lifshitz [18] derived an expression for the damping due to elastic wave radiation for a doubly clamped beam of length H and width w. Their model considers the support as a thin elastic plate of the same thickness as the beam, but of different width, and suggests $Q \sim H/w$ for the out-of-plane flexural mode. This would imply $Q \sim 10$ for our devices, which is clearly an underestimate. Another, perhaps more relevant expression was derived by Photiadis and Judge [19]. Their model considers a simple cantilever connected to a semi-infinite plate of thickness d_s. When the acoustic wavelength is long compared to the thickness of the support, the support losses are given by

$$Q^{-1}_{\text{attachment}} \approx 0.95 \frac{w}{H} \frac{d^2}{d_s^2} \left(\frac{\rho E}{\rho_s E_s} \right)^{1/2}, \tag{2.25}$$

where $\rho_s = 2300\,\text{kg/m}^3$ and $E_s \sim 100\,\text{GPa}$ are the density and elastic modulus of the (silicon) support. The proper elastic constant of the silicon depends on the axial direction of the stress. However, for the sake of estimations, the order of magnitude is sufficient. The thickness of the silicon chip $d_s = 500\,\mu\text{m}$ is small compared to the wavelength of sound $\lambda \approx 2\,\text{cm}$ at typical device frequency (300 kHz). With typical dimensions of the MEMS device ($H = 10\,\mu\text{m}$, $w = 1\,\mu\text{m}$, $d = 150\,\text{nm}$), we see that the support losses are rather small, resulting in $Q \sim 1 \times 10^8$. One should note that the lateral dimensions of the silicon chip (5 mm) are actually also smaller than the wavelength, so the assumption of semi-infinite plate is not strictly valid in our geometry. Damping due to elastic wave radiation is expected to be temperature independent.

Viscoelasticity in the context of boundary losses is related to the damping due to the material used to install the supporting structure in place (we use vacuum grease to attach the silicon chip). In our devices the mass of the silicon chip is nearly million times larger than the mass of the resonator and the motion of the resonator can not induce significant motion of the chip. Thus, viscoelastic damping is not relevant apart from being one of the possible mechanisms responsible for the damping of the

elastic waves radiated to the structure (complete dissipation of the elastic waves in the support structure is assumed in the derivation of Eq. (2.25)).

Microsliding could occur at the Al-SiO_2 or SiO_2-Si interfaces. However, the motion of our devices occur in the direction perpendicular to these interfaces and damping due to motional friction is unlikely. On the other hand, microsliding between the Al grains is possible and might contribute to the internal friction, which is discussed separately.

2.3.3 Internal damping

Internal damping occurs in the material of the resonator, and can be divided into two categories: fundamental damping and internal friction. In the internal dissipation mechanisms, the ordered mechanical energy is transformed into disordered internal energy of the system. Fundamental damping (thermoelastic damping, phonon-phonon interactions and phonon-electron interactions) set the ultimate lower limit on damping, and are present even in perfect crystals. Internal friction, on the other hand, is damping caused by irreversible motion of crystallographic defects (such as vacancies, edge dislocations and grain boundaries) and can be reduced by improving the crystal quality.

Material properties

To estimate the fundamental damping in the aluminium resonator, knowledge of certain physical properties is required. Especially, the heat capacity, thermal conductivity and thermal expansion coefficient of Al need to be characterized. Fortunately, the low temperature behaviour of these properties is fairly well known.

The specific heat of metals at low temperatures has contributions from electrons c_e and phonons c_p, so that $C = c_e + c_p$. In normal state, the expressions are

$$c_{en} = \gamma_{en} T \quad \text{and} \quad c_p = \frac{5}{12}\pi^4 R \left(\frac{T}{\theta_D}\right)^3, \tag{2.26}$$

where the constant γ_{en} is a material property, R is the universal gas constant and θ_D is the Debye temperature of the material. At sub-Kelvin temperatures, the phonon contribution to the heat capacity is typically small. The heat capacity of Al at $T < 1\,\mathrm{K}$ in the normal state is practically a linear function of the temperature with $\gamma_{en} = 1.35 \times 10^{-3}\,\mathrm{J/(mol \cdot K^2)}$ and the contribution from phonons (with $\theta_D = 427.7\,\mathrm{K}$) is smaller than 1% [20].

Since the heat is carried mostly by the electrons, the normal state thermal conductivity is well approximated by the Weidemann-Franz law

$$\kappa_H \approx \kappa_{en} = \sigma_e L_0 T, \tag{2.27}$$

where σ_e is the electrical conductivity and $L_0 = 2.443 \times 10^{-8}\,\mathrm{W\Omega/K^2}$ is the Lorentz number. The electrical conductivity is obtained by measuring the resistance of our devices ($R_{5\mathrm{NF}} = 0.6\,\Omega$ for sample 5NF) at low temperature (16 mK). The resistance is determined by a 4-wire method, where an off-resonant AC current is applied through the device and the change in the voltage over the device is measured when the superconductivity is suppressed with a small magnetic field ($\sim 40\,\mathrm{mT}$). The voltage change is assumed to result solely from the change in the resistance, and the normal-state resistivity is then given by the ratio of the voltage change and the AC current. With the known dimensions of the device, we get $\sigma_e = 7 \times 10^8\,\mathrm{S\,m^{-1}}$. The resistance of the device at room temperature is $40\,\Omega$ (measured with a multimeter) and the corresponding residual resistivity ratio (RRR) is 70. The RRR is one of the smallest values observed in Al of various purities [21]. The likely explanations for the low RRR are the small dimensions of the device and small grain size, which lead to large electron-boundary scattering.

Also the thermal expansion coefficient happens to be directly proportional to the specific heat at low temperatures [22]. Consequently, it has electronic and phononic contributions with the corresponding linear and cubic dependences. For aluminium at $T < 5\,\mathrm{K}$, the (normal state) linear thermal expansion coefficient is

$$\alpha_L = \alpha_e T + \alpha_p T^3, \tag{2.28}$$

where $\alpha_e = 9.3 \times 10^{-10}\,1/\mathrm{K^2}$ and $\alpha_p = 3.25 \times 10^{-11}\,1/\mathrm{K^4}$ [23]. Again, only the linear term is of importance at temperatures below 1 K.

Superconductivity has a significant effect on the specific heat of electrons, while the phonon contribution remains unchanged. When temperature is lowered past the superconducting transition temperature, the specific heat of electrons jumps to a higher value at the onset of the superconductivity and decreases exponentially, when temperature is decreased further. The measured electron specific heat in superconducting Al from 0.25 K to 0.5 K is approximately [20]

$$c_{es}(T) = 7.1\gamma_{en} T_c \exp(-1.34 T_c/T), \tag{2.29}$$

where $T_c = 1.163\,\mathrm{K}$ is the superconducting transition temperature. The available heat capacity data (down to 0.17 K [20]) does not allow for reliable extrapolation of c_{es} to very low temperatures. This is not of major concern, since the dominant contribution to the heat capacity at the lowest temperatures comes from phonons, whose heat capacity decreases more gradually with temperature. The electron heat capacity c_{es} becomes smaller than the phonon heat capacity c_p approximately at temperature $T_{eq} \approx 0.13\,\mathrm{K}$. Similar features are observed in the electronic heat conductivity, which follows [21]

$$\kappa_{es}(T) = \kappa_0 \exp\left[1.8\left(1 - \frac{T_c}{T}\right)\right] \quad \text{at} \quad T \gtrsim 0.2\,\mathrm{K}, \tag{2.30}$$

where κ_0 is the heat conductivity at T_c. As with the heat capacity, the phonon contribution becomes important at the lowest temperatures. Suffice it to say, superconductivity has an effect on the thermal expansion as well, and the change in length

between the superconducting and normal state Al may be expressed approximately by $(l_s - l_n)/l_s = (6.2 - 5.5T^2 - 0.7T^4) \times 10^{-9}$ [24].

Fundamental damping

Two fundamental damping mechanisms are considered here, thermoelastic damping (TED) and Akhiezer damping. TED is related to coupling between elastic and temperature fields and Akhiezer damping considers phonon-phonon interactions.

When a beam bends, it produces stress and strain gradients in the structure, so that one side of the beam will be in compression and the other in tension. Due to thermoelasticity, the compressed region becomes hotter and the tensioned region colder than the average temperature. The temperature gradient leads to irreversible heat flow and entropy generation. The resulting loss mechanism is called thermoelastic damping (TED). The theory for TED in a homogeneous, isotropic, Euler–Bernoulli beams was first established by Zener [25]. The resulting Q-value is obtained from equation

$$Q_{\mathrm{TED}}^{-1} = \frac{\alpha_L^2 ET}{C} \frac{\omega\tau_{\mathrm{TED}}}{1 + (\omega\tau_{\mathrm{TED}})^2}, \tag{2.31}$$

where $\tau_{\mathrm{TED}} = (d^2 C)/(\pi^2 \kappa_{\mathrm{H}})$ is the thermal diffusion time over the thickness of the beam. Considering only the linear (electronic) contributions to the heat capacity $C = \gamma_{en} T$ and thermal conductivity $\kappa_H = \sigma_e L_0 T$ in normal state Al, we find a temperature independent $\tau_{\mathrm{TED}} = 1.8 \times 10^{-14}\,\mathrm{s}$. For typical device frequency $\omega = 2\pi \times 300\,\mathrm{kHz}$ the product $\omega\tau_{\mathrm{TED}} = 3.4 \times 10^{-8}$ is small, and the expression for TED in the normal state at low temperatures becomes

$$Q_{\mathrm{TED}}^{-1} = \frac{\alpha_e^2 E \omega d^2}{\pi^2 \sigma_e L_0} T^2, \tag{2.32}$$

where the linear approximation $\alpha_L = \alpha_e T$ of the thermal expansion coefficient has been used. The Q values obtained from the expression are extremely high (e.g. $Q_{\mathrm{TED}} \sim 1 \times 10^{17}$ at $T = 1\,\mathrm{K}$).

Akhiezer damping [26] occurs due to irreversible heat flow between different phonon modes. The heat flow is driven by temperature differences arising from coupling of the strain field to the thermal phonons, which changes the frequency of the phonons. Generally speaking, the dimensionless coupling strength (also called the Grüneisen parameter) depends on the phonon mode. To a first approximation, the average value $\gamma_{\mathrm{av}} \approx 1.7$ [27] can be used for Al. In an approximation, where all the phonon modes have common thermal relaxation time τ_{Akhiezer}, the loss is given by [28, 29]

$$Q_{\mathrm{Akhiezer}}^{-1} = \frac{CT\gamma_{\mathrm{av}}^2}{\rho c^2} \frac{\omega\tau_{\mathrm{Akhiezer}}}{1 + (\omega\tau_{\mathrm{Akhiezer}})^2}, \tag{2.33}$$

where $c = 5100\,\mathrm{m/second}$ is the speed of sound in Al and $\tau_{\mathrm{Akhiezer}} = (3\kappa_{\mathrm{H}})(Cc^2)$. In normal state with the linear dependences of thermal conductivity and heat capacity,

the relaxation time is $\tau_{\mathrm{Akhiezer}} \approx 15\,\mathrm{ns}$. The product $\omega\tau_{\mathrm{Akhiezer}} = 0.028$ is much smaller than one, and the expression for Akhiezer damping at low temperature becomes

$$Q^{-1}_{\mathrm{Akhiezer}} = \frac{3\gamma^2_{\mathrm{av}}}{\rho c^4}\omega\sigma_e L_0 T^2, \tag{2.34}$$

which gives $Q_{\mathrm{Akhiezer}} \sim 2 \times 10^{10}$ at $T = 1\,\mathrm{K}$.

One should note, that at low temperatures ($T < 1\,\mathrm{K}$) the electron-phonon coupling is weak, and the electron temperature T_e may be substantially larger than that of the phonons (lattice) T_p even at very low excitation currents [30]. The loss mechanisms described above (TED and Akhiezer damping) are directly related to phonons and in the limit of zero heat exchange between electrons and phonons, the properties attributed solely to phonons should be used. Since the expected losses from TED and Akhiezer damping are extremely low and the Q-value of our our devices is clearly limited by other mechanisms, we do not consern ourselves further with these issues.

Internal friction

The magnitude of the internal friction can not typically be estimated from first principles, but generally it depends on the type, distribution and mobility of defects and interactions between the different classes of the defects [16]. Single-crystal materials can be used to obtain high Q, or the material can be annealed at an elavated temperature to increase the grain size, which is found to reduce damping. Another strategy involves reducing mobility of the defects, which depend on atomic bonding, crystal structure, microstructure, melting temperature, operating temperature and frequency. Small quantities of alloying can reduce defect mobility, which may have a significant effect on Q. For example, damping in aluminium alloy Al 5056 is an order of magnitude smaller than in pure Al over a wide temperature and frequency ranges.

At low temperatures, the internal friction in many MEMS and NEMS resonators is believed to result from tunneling two level systems (TLSs) present in the devices, which are typically attributed to amorphous materials [31, 32]. The damping is explained in the framework of the standard tunneling model (STM) [33]. Many MEMS/NEMS resonators have a polycrystalline metal layer either as the mechanical structure or as a metallic coating. TLSs can reside at the internal boundaries or at the surfaces due to imperfect termination of the crystals. Note that many metals (such as aluminium) also form an amorphous native oxide layer when they are subjected to atmospheric conditions. The basic idea is that a TLS can exist in one of two minima in a double-well potential (which need not be symmetric), separated by an energy barrier (e.g. an atom with two favourable locations). At low enough temperatures, thermal activation over the barrier is suppressed and the dynamics of the TLS is governed by quantum tunneling. In a system of many TLSs,

there exists a wide distribution of potential barrier heights, relaxation rates and eigenenergies.

In a mechanical resonator, the TLSs couple to the applied strain fields induced by the motion of the device and absorb energy from the mechanical mode. The energy is then redistributed among the rest of the degrees of freedom of the system (phonons, electrons or other TLS). In resonant dissipation, the TLSs with excitation energy E_{TLS} close to the energy $\hbar\omega$ will resonate with the vibrational mode. For typical oscillation amplitudes, the vibrational mode is so populated compared to the thermal population that the resonant TLSs become saturated and their contribution to the dissipation becomes negligible [34]. However, the resonant mechanism is responsible for a shift in resonance frequency (or sound velocity $\omega_0 \propto c = \sqrt{E/\rho}$), which is in the limit $\hbar\omega \ll k_B T$ given by [33]

$$\frac{\delta\omega_0}{\omega_0} = \frac{P_0\gamma_c^2}{E}\ln(T/T_0), \tag{2.35}$$

where T_0 is a reference temperature, ω_0 is the resonance frequency at the reference temperature, $\delta\omega_0$ is the frequency shift, P_0 is the density of states and γ_c is a coupling constant between the phonons and the TLSs. The effect is insensitive to the strength of the elastic field, since a major contribution to the frequency shift comes from states with energy near $k_B T$, which are not easily saturated by the oscillations of the device, which operates at a much lower frequency.

The relevant damping mechanism due to TLSs in mechanical resonators is the relaxation absorption [33]. In thermal equilibtrium at temperature T, the ratio of the occupation probabilites of the two energy levels of a TLS is $\exp(-E_{TLS}/k_B T)$. Since the wavelength of phonons $\sim 100\,\mathrm{nm}$ is long compared to the size of the TLSs $\sim 1\,\text{Å}$, the local strain field at any one TLS can be taken as uniform (dipole approximation). The main effect of this uniform elastic field is to modulate the energy of the TLS, which in turn leads to an unequilibrium of the populations (occupation probabilities). The relaxation of the populations towards the equilibrium value is typically slow compared to the rate of change ω of the elastic field. As a response to the elastic forcing, the TLSs produce a complex modulus, which is analoguous to the electrical susceptibility. The frequency shift and dissipation due to the TLSs are proportional to the real and imaginary parts of the complex modulus, respectively. Unlike the resonant mechanism, the relaxation absorption is not easily saturated as it does not directly drive transitions of the TLSs.

The minimum relaxation time for the states with $E = k_B T$ is temperature dependent with $\tau_{\min} \propto T^{-3}$ and $\tau_{\min} \sim 1\,\mathrm{ns}$ at $T = 1\,\mathrm{K}$ in bulk amorphous insulators. Above $1\,\mathrm{K}$ the simple power-law dependence of the minimum relaxation time breaks down, as higher order phonon processes become important. The relaxation absorption then leads to a temperature-dependent damping $\propto T^3$ at low temperatures (when $\omega\tau_{min} \gg 1$) and a constant damping at high temperatures (when $\omega\tau_{\min} \ll 1$). A transition from one dependence to the another is expected at some temperature T^*, when $\omega\tau_{\min} \sim 1$.

When $\omega\tau_{min} \gg 1$, the resonant process dominates the frequency shift and the relaxation process is not important. For $\omega\tau_{min} \ll 1$ and $\hbar\omega \ll k_B T$, the relaxation mechanism produces a negative frequency shift [33]

$$\frac{\delta\omega_0}{\omega_0} = -\frac{3}{2}\frac{P_0\gamma_c^2}{E}\ln(T/T_0), \tag{2.36}$$

which is 3/2 times larger the the shift due to the resonant mechanism. As a consequence, the frequency shift should show a maxima approximately when $\omega\tau_{\min} \sim 1$, which occurs around the temperature T^*.

In metallic glasses, the minimum relaxation time is much shorter and it is inversely proportional to the temperature. The resulting relaxation damping in the low temperature limit $\omega\tau_{\min} \gg 1$ is directly proportional to the temperature, while the effect on the frequency is negligible [33]. Since the upper limit for the relaxation time is 25 ns even at $T = 10$ mK, the temperature dependent low temperature region of damping in metallic glasses is hard to achieve (or required devices with high frequency). The damping is constant at high temperatures ($\omega\tau_{\min} \ll 1$) and the result is equivalent to the result in amorphous insulators, since the mechanism does not depend on the relaxation time. The corresponding frequency shift in the high temperature limit ($\omega\tau_{\min} \ll 1$) contains contributions from the resonant and relaxation mechanisms, and the combined effect is

$$\frac{\delta\omega_0}{\omega_0} = \frac{1}{2}\frac{P_0\gamma_c^2}{E}\ln(T/T_0), \tag{2.37}$$

where the factor 1/2 is the sum of the resonant term 1 and the relaxation term $-1/2$. At higher temperatures, the phonons take over the electron contribution as the dominant source of relaxation and in principle, a logarithmic decrease in frequency would be expected. In practice, higher order phonon processes modify the logarithmic dependence to give an almost linear decrease of frequency with temperature [33]. Typically, the maximum frequency is observed between 2 K and 3 K in metallic glasses. The temperature of the maximum is almost frequency independent, unlike in insulating glasses, where T^* scales as $\omega^{1/3}$.

Common features are observed in many MEMS/NEMS resonators, whose quality factor is limited by tunneling two level systems. Below a threshold temperature T^* the dissipation follows a power law $Q^{-1} \propto T^N$ and at higher temperatures a rather flat dependence on temperature is observed. The frequency shift increases logarithmically below T^* and shows a maxima around this threshold temperature. However, the measured exponents for various NEMS/MEMS resonators show large variation between $N = 0.32$ and $N = 1.6$ [35, 36, 37, 38, 39, 40, 41, 42], and many of the results are hard to explain in the framework of tunneling two level systems. In confined dimensions, when the phonon wavelengths become longer than the devices, modifications to the theory of tunneling TLS are required. Note that the electrons remain 3D practically in all devices. A fairly general review article on TLSs in reduced dimensions is given in [43]. Quite interestingly, TLSs couping to

1D phonon modes in a tensioned string ($\omega \propto k_\lambda$) produce qualitatively ($N = 1$) and quantitatively the observed behaviour in normal state doubly clamped aluminium nanobeams [38], while the (qualitatively correct) electron mediated mechanism gives values of the relevant parameters, which are inconsistent by several orders of magnitude. The result implies that the polycrystalline aluminium nanobeams behave more like amorphous insulators than amorphous metals. The $N = 1$ behaviour has been observed in superconducting aluminium nanobeams as well [39], consistent with the 1D phonon picture. Seoánez et al. [34] predict $N = 1/2$ for pure flexure ($\omega \propto k_\lambda^2$) and 1D phonons, which matches closely the measured dependence $N = 0.5 \pm 0.05$ for doubly clamped gold nanowires in [36]. The prediction is also close to the normal-state result $N = 0.65 \pm 0.1$ for goalpost shaped silicon resonators, which are covered with aluminium [37]. However, the same devices show very different behaviour in the superconducting state with $N = 1.5 \pm 0.1$, which implies that the normal-state electrons play a crucial role in the dissipation. The result is then in contradiction with the 1D phonon picture. The low values $N = 0.32$ for a GaAs nanobeam in [40] and $N = 0.36$ for a single-crystal Si nanobeam (covered with chromium and gold) in [35] and the high value $N = 1.6$ in single crystal diamond (no metallic coating) [41] remain unexplained as well.

The choise of dispersion relation (1D, 2D or 3D) of phonons depends on the dominant phonon wavelength $\lambda_{\mathrm{ph}} = hc/(2.82k_BT)$, where c is the speed of sound. If one (or two) dimension of the device is smaller than the phonon wavelength, the 2D (or 1D) model should be used. For our devices, λ_{ph} becomes equal to the thickness $d = 150\,\mathrm{nm}$ at $T = 6\,\mathrm{K}$ and width $w = 1\,\mu\mathrm{m}$ at $T = 1\,\mathrm{K}$. Thus, the phonons will cross over from 3D to 1D as temperature is lowered. On the other hand, the fermi wavelength is small ($< 1\,\mathrm{nm}$) and electrons remain 3D at all temperatures. The mechanical out-of-plane resonance mode of our devices is flexurar ($\omega \propto k_\lambda^2$). For $1D$ phonons and a flexural resonance mode, the quantitative formula for the damping is given by [34]

$$Q_{\mathrm{rel}}^{-1} = \frac{10P_0\gamma_c^4}{d^{3/2}w}\frac{(1+\nu)(1-2\nu)}{E^2(3-5\nu)}\left(\frac{\rho}{E}\right)^{1/4}\frac{T^{1/2}}{\omega_0}, \tag{2.38}$$

where $P_0 \sim 10^{44}\mathrm{J}^{-1}\mathrm{m}^{-3}$ is the density of states of the TLS (a general, constant value attributed to amorphous insulators is assumed here), $\gamma_c \sim 1\,\mathrm{eV}$ is the coupling constant between the elastic modes and the TLS and $\nu = 0.334$ is the Poisson's ratio of aluminium. The fraction of amorphous material is assumed to be 5%, which corresponds to the expected thickness 3 nm [44] of the native aluminium oxide layer. In the derivation of the aforementioned equation, the convention $\hbar = 1 = k_B$ has been used. Based on simple dimensional analysis, the result should be multiplied with the factor $k_B^{1/2}/\hbar^{3/2}$ to get the proper dimensionless loss factor. For typical device dimensions and frequency ($d = 150\,\mathrm{nm}$, $w = 1\,\mu\mathrm{m}$, $\omega_0 = 2\pi \times 400\,\mathrm{kHz}$) and a moderate coupling constant $\gamma_c = 3\,\mathrm{eV}$, the model fives $Q \sim 1 \times 10^4$ at $T = 10\,\mathrm{mK}$. Measurements in the superconducting state can possibly provide more information regarding the relaxation mechanism of the TLSs (section 4).

To complete the discussion on TLSs in these systems, also the possibility of a tem-

perature dependent TLS density of states should be considered. Behunin et al. [43] suggest that the low temperature ($\omega\tau_{\min} \gg 1$) dissipation is proportional to $T^{D+\mu}$, where D (1, 2 or 3) is the dimension and μ is related to the TLSs density of states through $P(k_BT) \propto T^{\mu}$. At high temperatures ($\omega\tau_{\min} \ll 1$) the dissipation is proportional to T^{μ}, which provides an indirect window to study the DOS of the TLSs. Finally, devices which support flexural modes show entirely different behaviour. Their dissipation follows $Q^{-1} \propto T^{1/2+\mu}$ (1D), $Q^{-1} \propto T^{1+\mu}$ (2D) or $Q^{-1} \propto T^{3+\mu}$ (3D) at low temperature and T^{μ} at high temperature .

Behunin et al. suggest that the small exponents $N = 0.36$ observed in [35] could be explained by the high temperature ($\omega\tau_{\min} \ll 1$) behaviour $Q^{-1} \propto T^{\mu}$. This would put the $\sim 10\,\mathrm{MHz}$ device (single crystal nanobeam, which is covered with chromium and gold) in the limit $\omega\tau_{\min} \ll 1$ at temperatures as low as 100 mK. The upper limit for the corresponding minimum relaxation time would be $\tau_{min}(100\,\mathrm{mK}) < 16\,\mathrm{ns}$. This interpration seems to contradict with our results, which show distinct low and high temperature behaviours with a crossover around 1 K, which implies $\tau_{\min}(1\,\mathrm{K}) \sim \omega_0^{-1} \approx 400\,\mathrm{ns}$. Even longer relaxation times are expected at lower temperatures.

As the above discussion shows, the dissipation in some NEMS/MEMS devices can be explained in the framework of tunneling two level systems either qualitatively or quantitatively. However, many of the results remain inconsistent with theory. Revision of the basic ideas of the tunneling two level systems have been suggested in [45] even for the amorphous materials. Measurements on many different geometries, frequencies and materials are required to build a consistent picture of the mechanism. Compared to the other nanoscale devices, our devices operate at a very low frequency. Tunneling TLS losses in such a low frequency device with confined 1D phonons have not been reported before.

2.4 Fluid drag

This section considers the possible drag forces arisin in superfluid ^{4}He, with a focus on the effects below 1 K temperature. Suffice to say that at higher temperatures the the force experienced by oscillators moving through the fluids is mainly due to viscous drag and potential flow [3]. Unfortunately, the drag experienced by our devices at $T > 1\,\mathrm{K}$ is so high that the signal from the devices is too small to detect even at the highest driving forces. Consequently, experiments were conducted only at temperatures below 1 K. Future experiments in the high temperature regime are possible, but they will likely require a stronger magnetic field to be conducted.

When an oscillating body moves through a fluid at a small velocity, it experiences a force with components proportional to its velocity $\dot{x}$ (drag) and acceleration $\ddot{x}$ (mass enhancement):

$$F_{\text{fluid}} = \lambda_{\text{fluid}}\dot{x} + \tilde{m}\ddot{x}. \tag{2.39}$$

The addition of the force to the equation of motion causes a negative shift in the resonance frequency

$$\left(\frac{\omega_{\text{fluid}}}{\omega_{\text{vac}}}\right)^2 = \frac{m_0}{m_0 + \tilde{m}} \tag{2.40}$$

and a change in the damping coefficient

$$\gamma = \gamma_{\text{int}} \frac{m_0}{m_0 + \tilde{m}} + \frac{\lambda_{\text{fluid}}}{m_0 + \tilde{m}} = \gamma_{\text{int}} \left(\frac{\omega_{\text{fluid}}}{\omega_{\text{vac}}}\right)^2 + \gamma_{\text{fluid}}. \tag{2.41}$$

At temperatures $T < 1\,\text{K}$, the fraction of normal fluid in liquid ^{4}He is vanishingly small and the viscocity is negligible. In an inviscid fluid, the mass enhancement is solely due to the potential flow of the liquid around the body. The frequency shift for a (long and thin) rectangular cantilever oscillating at a small amplitude ($x_0 \ll d$) due to an inviscid fluid was first derived by Chu [46] and is given by

$$\left(\frac{\omega_{fluid}}{\omega_{\text{vac}}}\right)^2 = \left(1 + \frac{\pi w}{4d} \frac{\rho_{\text{fluid}}}{\rho_{\text{cantilever}}}\right)^{-1}. \tag{2.42}$$

The expression predicts a 12% decrease in resonance frequency in ^{4}He at 3 bar pressure at low temperature for the typical device dimensions ($d = 150\,\text{nm}$ and $w = 1\,\mu\text{m}$).

2.4.1 Ballistic drag

Phonons and rotons are collective excitations of the superfluid ^{4}He [47] and produce the dispersion relation shown in Fig. 2.5 [48]. Excitations with a low momentum have a linear dispersion relation, and are called phonons. The slope of the linear relation corresponds to the velocity of sound in the liquid. Excitations around the local minimum in energy at the wavenumber k_0 are called rotons, and the energy of the minimum Δ_{rot} is the roton gap. The exact shape of the dispersion curve depends on temperature and pressure.

The response of the devices have been measured in superfluid ^{4}He at 3 bar pressure. The corresponding density is $\rho_{4\text{He}} = 150\,\text{kg/m}^3$ [49] and the velocity of sound is $c = 260\,\text{m/s}$ [50]. Changes in the velocity of sound as a function of temperature below $T = 1\,\text{K}$ are expected to be small ($< 1\,\text{m}\,\text{s}^{-1}$) [51]. The location of the roton minimum $k_0 = 1.93\text{Å}^{-1}$ is temperature independent, but increases with the cubic root of the density [52]. At zero temperature and with the density $\rho_{4He} = 150\,\text{kg/m}^3$, the value of the roton gap is $\Delta_{\text{rot}} = 8.40\,\text{K}$ [53]. At $T \lesssim 1\,\text{K}$, the value of the roton gap depends only weakly on temperature. A small decrease ($\sim 0.5\%$) in the value of Δ_{rot} can be expected, when comparing the value at $T = 1\,\text{K}$ to the value at zero temperature [54].

The mean free path of the quasiparticles (phonon, roton) in superfluid ^{4}He at low temperatures are much larger than the transverse dimensions of the devices ($\sim 1\,\mu\text{m}$),

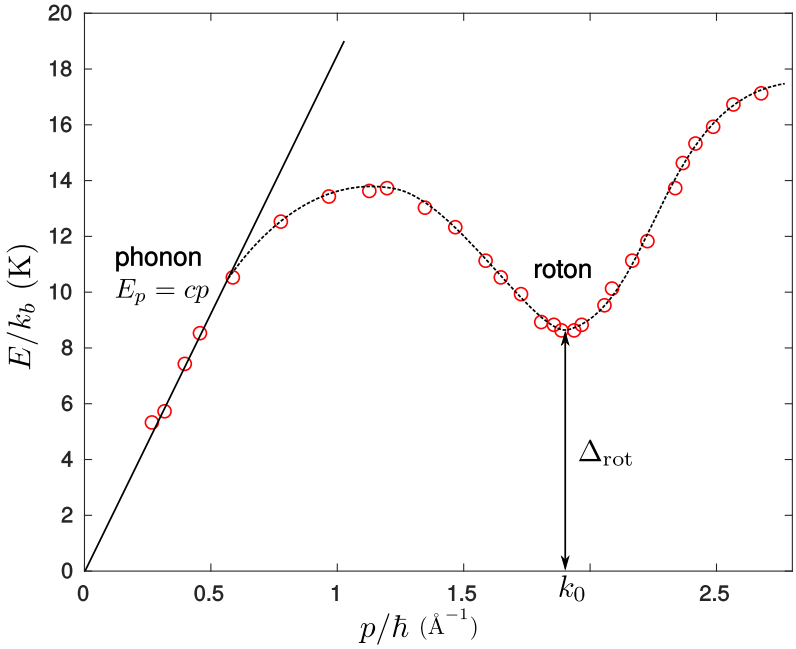

Figure 2.5: Dispersion relation of ^{4}He at $T = 1.12\,\mathrm{K}$ in saturated vapour pressure. The data (circles) has been obtained from [48]. The solid line is a fit to the low-momentum linear contribution attributed to phonons. The dashed line through the data at higher momentum is a quide to the eye, and shows the distinct roton minimum.

e.g. $l_{\rm mfp}(1\,\mathrm{K}) \sim 20\,\mu\mathrm{m}$ and $l_{\rm mfp}(0.7\,\mathrm{K}) \sim 300\,\mu\mathrm{m}$. At this temperature regime, the drag force experienced by the oscillator moving through the fluid is due to momentum transfer in collisions with the ballistic quasiparticles. The damping coefficients due to phonons and rotons are given by [55]

$$\gamma_{\rm ph} = \rho_{\rm ph} c\sigma/m \quad \text{and} \quad \lambda_{\rm rot} = \rho_{\rm rot}\bar{u}\sigma/m, \tag{2.43}$$

where $\rho_{\rm ph,rot}$ are the densities whereas c and $\bar{u}$ are the mean velocities of the quasiparticles, σ is the scattering cross section and $m = m_0 + \tilde{m}$ is the effective mass of the oscillator in the fluid. The wavelength of rotons ($2\pi/k_0 \approx 3$Å) is small, and the wavelength of the thermal phonons (ch/k_BT) becomes comparable to the transverse dimensions $\sim 1\,\mu\mathrm{m}$ only at very low temperatures $\sim 10\,\mathrm{mK}$. Thus, the scattering cross section is given by the projected area $A_p = w(2H + L)$ of the device in the y-z plane, normalized with the velocity profile

$$\sigma = \iint_{A_p} \frac{\dot{x}(y,z)}{\dot{x}_{\rm max}} dydz \approx 0.57w(2H + L). \tag{2.44}$$

Inserting the definitions for the phonon and roton properties, the expressions for the damping coefficients become [56]

$$\gamma_{\rm ph} = \frac{\sigma}{m}\frac{2\pi^2 k_b^4}{45\hbar^3 c^4} T^4 \tag{2.45}$$

and

$$\gamma_{\rm rot} = \frac{\sigma}{m}\frac{\hbar k_0^4}{3\pi^2}\exp\left(-\frac{\Delta_{\rm rot}}{T}\right). \tag{2.46}$$

2.4.2 Kelvin waves and vortex rings

Quantum turbulence (drag proportional to $\dot{x}^2$) [57] is expected, when oscillation velocity exceeds a critical velocity $v_{\rm crit}$. Assuming that the creation of quantum turbulence is associated with the excitation of Kelvin waves, the requirement is that the amplitude of the Kelvin waves exceed their wavelength. In absence of resonant amplification, this will occur when the oscillation amplitude of the mechanical resonator exceeds the Kelvin wavelength. Starting from Kelvin-wave dispersion relation

$$\omega = \frac{\kappa k_{KW}^2}{4\pi}\ln(1/k_{KW}a_0), \tag{2.47}$$

the critical velocity is given by [57]

$$v_{\rm crit} = A\left(\frac{\kappa\omega\ln(1/ka_0)}{4\pi}\right)^{1/2} \approx A'(\kappa\omega)^{1/2}, \tag{2.48}$$

where $\kappa = 9.97\times10^{-8}\,{\rm m}^2/{\rm s}^2$ is the circulation quantum (in ^{4}He), $a_0 \sim 1\,$Å is the core size, k_{KW} is the wavenumber of the kelvin waves, A and A' are numerical factors of order unity. With $A' = 1$ and $\omega = 2\pi\times300\,{\rm kHz}$, the result is $v_{\rm crit} \approx 43\,{\rm cm\,s^{-1}}$.

Another possible dissipation mechanism is emission of vortes rings. Oscillating spheres are known to emit vortex rings comparable to the size of the sphere. Considering rings of the size of the beam (radius $w/2$), their self-induced velocity is given by [58]

$$v_{\rm self} = \frac{\kappa}{2\pi w}\left(\ln\frac{4w}{a_0} - 1/2\right) \approx 16\,{\rm cm\,s^{-1}} \tag{2.49}$$

and the momentum (impulse) of such a vortex ring is [58]

$$P_{\rm ring} = \rho\kappa\pi(w/2)^2 \approx 1\times10^{-17}\,{\rm kg\,m\,s^{-1}}. \tag{2.50}$$

When a vortex ring detaches from the resonator, it gives a strong momentum kick, which can possibly be observed.

We mention here briefly also the mechanism, which we plan to study with these devices in the future. Assume that a vortex is coupled to the oscillator, so that it is stretched between two trapping sites, as shown in Fig. 2.6. One of the trapping sites will be on the beam of the oscillator and the other will reside nearby, at a distance corresponding to the Kelvin wave wavelength at the device frequency. No one knows the exact magnitude of the dynamic force that the oscillating Kelvin wave exerts on the device, but an upper limit is given by the tension of a vortex line

$$F_t = \frac{\rho_{He}\kappa^2}{4\pi}\ln\left(\frac{R_v}{a_0}\right) \sim 1\,{\rm pN}, \tag{2.51}$$

where R_v is the outer dimension of the vortex. This is approximately 100 times larger force than the expected force sensitivity presented in section 2.2.1. Thus, these devices may be sensitive enough to measure the dynamics of a single vortex line. We also plan to use the other half of the trapping site as a gate voltage (see Fig. 2.6), which will allow us to tune the resonance position and nonlinearity (through nonlinear coupling to the gate).

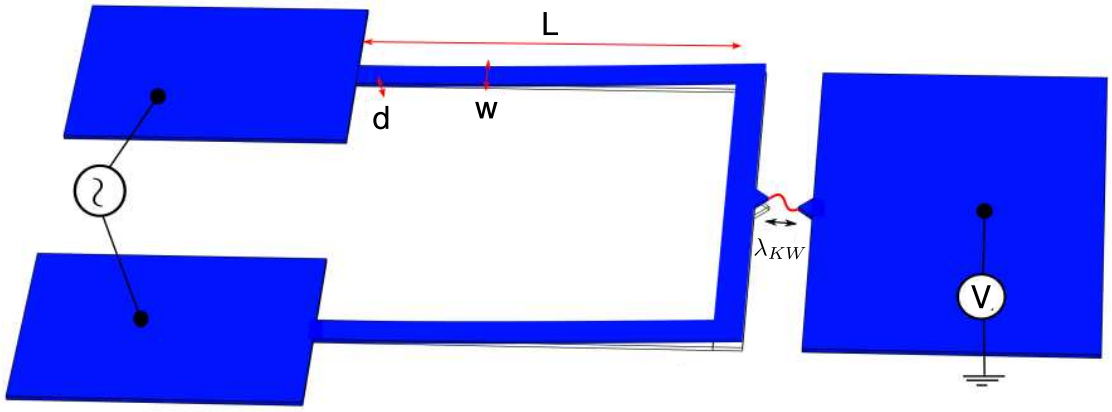

Figure 2.6: A schematic picture of the planned device with a trapping site for a vortex. The other half of the trapping site will also function as a gate with the applied voltage V.

2.4.3 Acoustic emission

Since the devices operate at a relatively high frequency, considerable losses could arise due to acoustic emission. The acoustic wavelength in ^{4}He at the device frequency $\lambda_{He} \sim 1\,\mathrm{mm}$ is large compared to the device dimensions, and the oscillating paddle can be described as a dipolar acoustic source, where the distance between the point sources is the width of the beam. The resulting loss factor is [59]

$$Q_{ac}^{-1} = \frac{L^2 w^4 \omega_0^3 \rho_{He}}{6\pi c^3 m_0}. \tag{2.52}$$

For typical device frequency $\omega_0 = 2\pi \times 300\,\mathrm{kHz}$, dimensions ($w = 1\,\mu\mathrm{m}$, $L = 10\,\mu\mathrm{m}$) and mass $m_0 = 10\,\mathrm{pg}$, the expression gives $Q_{ac} \sim 3 \times 10^7$. Changes in the velocity of sound are expected to be small at low temperatures, and the effect is assumed to be temperature independent.

Chapter 3

Research methods

In this chapter, the fabrication of the devices, the measurement circuitry, and the low temperature setup are described.

3.1 Fabrication

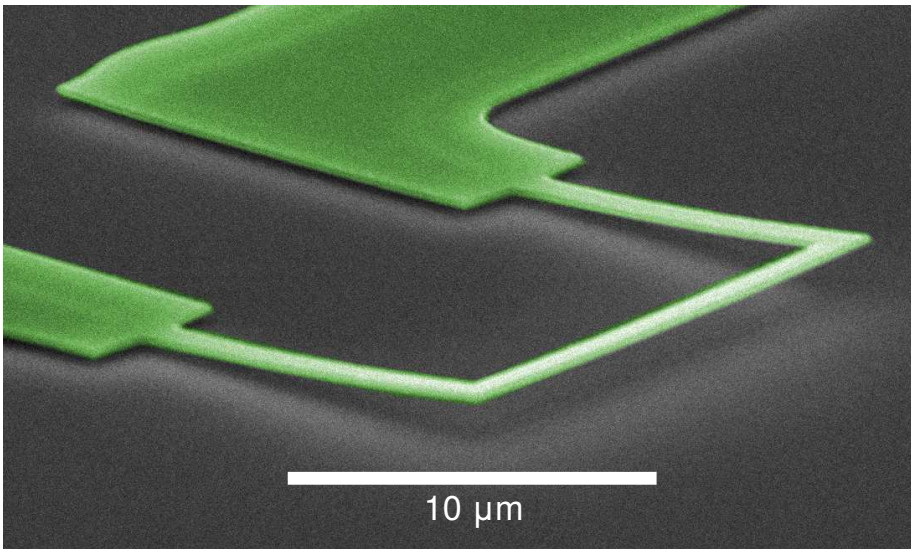

Figure 3.1: A false-colour SEM micograph of sample 4GN. Note how the device is clearly bent upwards from the silicon surface.

The test devices are suspended aluminium MEMS resonators with $\sim 10\,\mu m$ dimensions and rectangular cross section of $0.15\,\mu m \times 1.0\,\mu m$ (see Fig. 3.1). The fabrication process has been described in more detail in [12], but we shall briefly recap it here. A schematic presentation of the fabrication process can be seen in Fig. 3.2. The devices are fabricated on high purity (resistivity $> 100\,\Omega m$) silicon chips with 275 nm thick SiO_2 sacrificial layer on top. A PMMA bilayer, acting as a positive resist, is spin

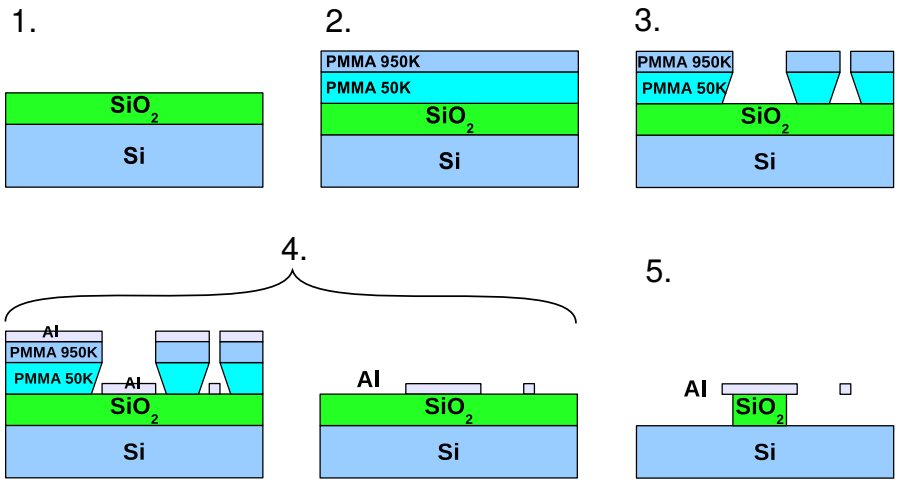

Figure 3.2: Schematic pictures (side view, not to scale) of the chips after each step in the fabrication process: 1. Cleaning, 2. Resist spin coating, 3. Electron Beam lithography and resist development, 4. Electron beam evaporation and lift-off, 5. HF-vapour etching.

coated on top of the chips and the devices are patterned by means of electron beam lithography. The aluminium layer is deposited with an electron beam evaporator and the free-standing structures are released with dry HF-vapour etching.

The different thermal expansion coefficients of Si, SiO and Al give rise to large static stress and strain in the structures. The strain can be observed even at room temperature, where it causes bending of the devices away from the Si surface (see fig. 3.1). The typical grain size in the Al film is $\sim 50\,\mathrm{nm}$ and the roughness of the surface and edges is $\sim 10\,\mathrm{nm}$ [12].

3.2 Measurement scheme

The MEMS devices are measured with a four-wire measurement, as shown in Fig. 3.3. The excitation current I_{ext} through the device is produced by an arbitrary waveform generator V_{ext}, followed by a 40 dB or 80 dB attenuator and a resistor $R \sim 1\,\mathrm{k}\Omega$ connected in series with the MEMS device. The MEMS device is described with the equivalent RLC circuit, as discussed in section 2.3.1. The inductor L_w and resistor R_w stand for the self inductance and (normal state) resistance of the device. The capacitor C_s stands for the combined stray capacitance of the signal wires, the output of the generator and the input of the preamplifier. R_i is the resistance of the signal input of the preamplifier. The impedance of the device is small and stray current I_s through the stray capacitance C_s and input resistance R_i is assumed to be small.

A superconducting coil magnet (inner diameter 18 mm, length 15 mm) provides a magnetic field ($83.5\,\mathrm{mT\,A^{-1}}$ at the center of the magnet) enabling the magneto-

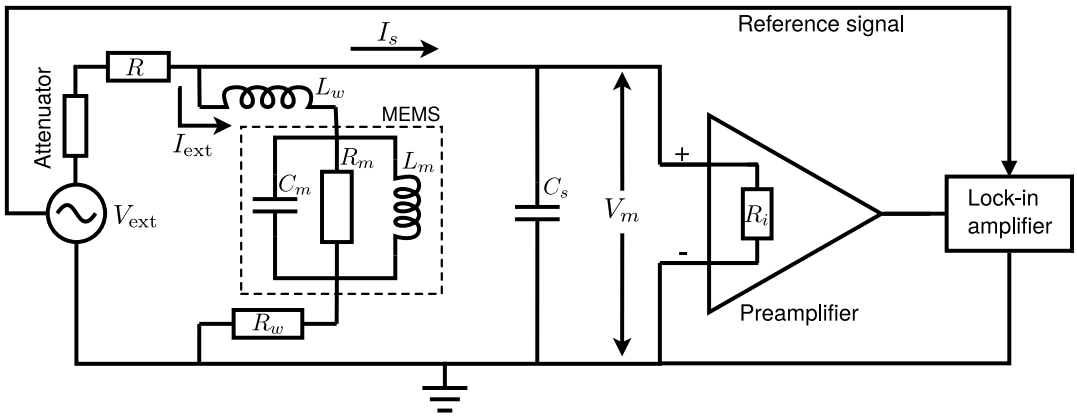

Figure 3.3: A circuit diagram describing the measurement of the MEMS devices. The MEMS device is depicted with the equivalent RLC circuit.

motive measurement scheme. The positioning of the samples inside the magnet is assumed to be accurate within 2 mm of the center of the magnet, where the field inhomogeneity is calculated to be less than 2.5%. The motion of the device through the magnetic field induces a voltage, which is amplified with the preamplifier connected parallel with the MEMS device. The amplified signal is then measured with a lock-in amplifier, which is phase locked with the voltage source through the reference signal.

The response of the devices is measured by sweeping the frequency of the excitation current over the mechanical resonance while measuring the voltage over the device. The measured voltage V_m is a sum of the induced voltage V and a background signal V_{bg} arising due to the self inductance L_w, (normal state) resistance R_w of the wire and other effects which are not captured by the simple circuit diagram. In practice, the full background signal observed in wide frequency sweeps ($\sim 100\,\text{kHz}$) is rather complicated, involving many apparent resonance peaks of electrical origin. The peaks can be distinguished from the mechanical resonance since they do not change as a function of the magnetic field, temperature, or due to immersion in superfluid. Additionally, their amplitude is typically few orders of magnitude higher than expected from the meachanical resonator and their Q is fairly low ~ 100. For sufficiently narrow sweeps (high Q of the mechanical resonator), the background signal is essentially a linear function of the frequency, and it is subtracted from the measured response. At temperatures near 1 K in superfluid ^{4}He, the mechanical resonance is wide ($\sim 10\,\text{kHz}$) and a quadratic background reduction is used.

Typically, a time constant 300 ms of the lock-in amplifier is used, and the noise in the amplified (500x) signal is $\sim 2\,\mu\text{V}$, which corresponds to $\sim 4\,\text{nV}$ noise in the original signal. For the typical magnetic field $B = 83\,\text{mT}$, deflection $x_0 = 10\,\text{nm}$, beam length $L = 10\,\mu\text{m}$ and frequency $\omega = 2\pi \times 300\,\text{kHz}$, the generated voltage obtained from Eq. (2.5) is only 16 nV. Signal averaging is obviously required for measuring the smallest deflections accurately.

3.3 Low temperature setup

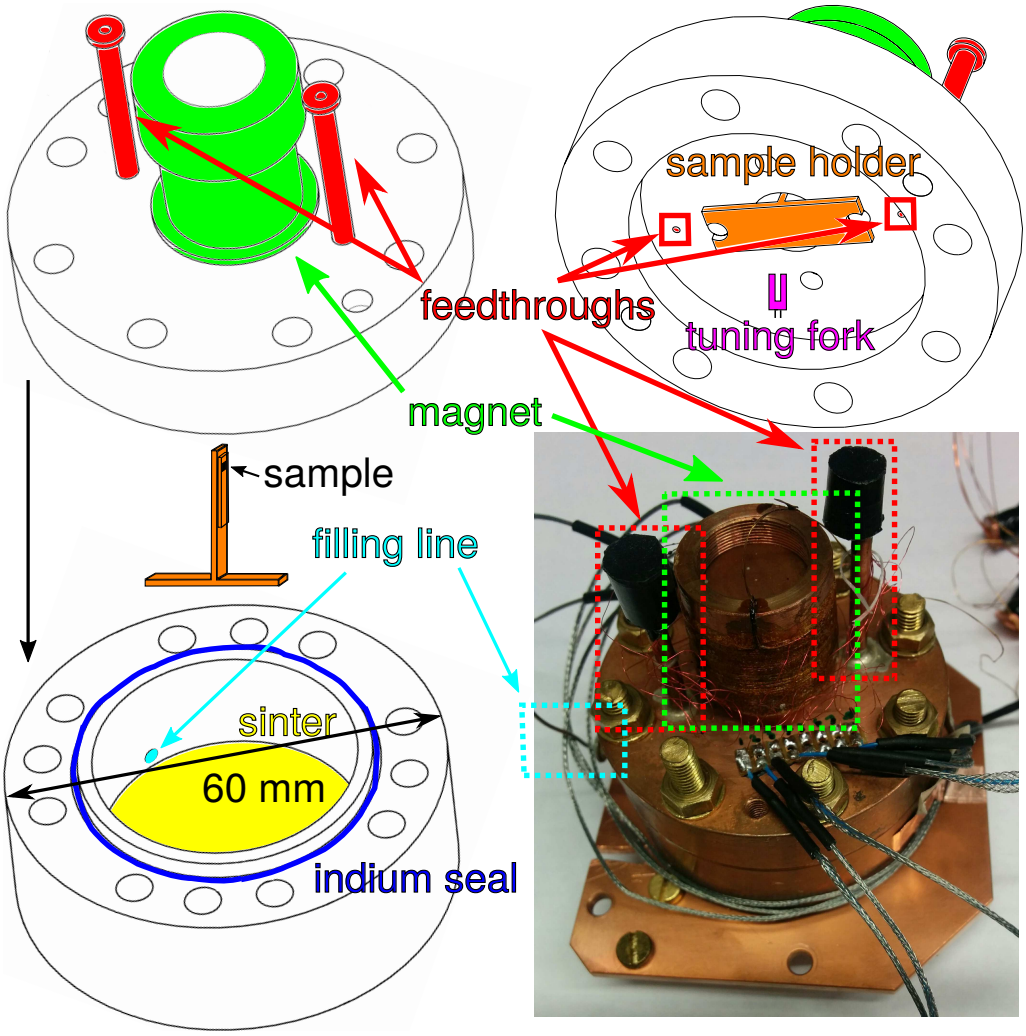

Figure 3.4: Schematic pictures of the copper container: top part of the container, view from top (top left), view from bottom (top right), bottom part of the container (bottom left) and a photograph of the assembled container (bottom right). The sample holder (shown in orange colour in the schematic figures) carries the sample chip, which is installed at the center of the superconducting coil magnet (green). A quartz tuning fork (magenta) is used as a reference device. The signal wires go to the container through the feedthroughs (red), which are sealed with Stycast (the black blobs at top of the feedthroughs in the photograph of the assembled container). Indium (blue) is used between the two parts of the container for a leak-tight seal. The container can be pumped to vacuum and filled with helium through the filling line (cyan). When the container is filled, the sintered surface (yellow) ensures a good thermal contact between the liquid and the bottom of the container even at the lowest temperatures. The container is bolted to a plate, which is installed to the mixing chamber stage of a dilution refrigerator.

To reach milliKelvin temperatures, the devices are installed in a copper container (Fig. 3.4), which is attached to the mixing chamber stage of a Bluefors LD-400 dry dilution refrigerator [60] with base temperature $\sim 10\,\mathrm{mK}$. The temperature of the mixing chamber stage is monitored with a resistive ruthenium oxide temperature sensor (Lake Shore Cryotronics, inc. RX-102B), whose resistance is measured with a Lake Shore model 370 resistance bridge. The expected accuracy in temperature is $\Delta T = \pm 2\,\mathrm{mK}$ at the lowest temperatures, while the error increases to $\Delta T = \pm 16\,\mathrm{mK}$ around $T \sim 1\,\mathrm{K}$ [61]. A quartz tuning fork (model ECS-.327-8-14X), removed from its original vacuum housing, is installed inside the copper container and acts as an additional temperature monitor operating directly in the liquid ^{4}He when the container is filled. To control the temperature, we use a resistive heater ($120\,\Omega$), attached to the dilution refrigerator, which provides continuous cooling. A PID controller is used to stabilize temperature (when not measuring at the base temperature), while simple current sweeps through the heater are used to make slow temperature sweeps.

Altogether 14 signal wires going to the container enable measurements of three MEMS devices (4 wire measurement) and a tuning fork (two wires). Two of the MEMS devices are connected to twisted pair wires (phosphor bronze), while the third device (5NF) and the quartz tuning fork are connected to thermocoax wires of the cryostat. Standard coaxial cables are used for connecting the measurement equipment to the wiring of the cryostat in room temperature. One of the MEMS devices (5NN) suffered from a bad connection (apparently one of the wire bonds broke), but we were still able to measure the resonance response of the device with the three connected wires (by connecting grounds in room temperature), albeit at a cost of increased background signal.

Chapter 4

Results

In this chapter the response of the MEMS devices, measured in vacuum at temperatures from 16 mK to 4 K and in superfluid ^{4}He at 3 bar pressure from 18 mK to 1 K, are presented, and the results are discussed. The dimensions and measured properties of the devices are given in Table 4.1. Most of the dimensions are measured from SEM micrographs, while the thickness d is taken from the crystal film thickness monitor of the electron beam evaporator. The dimensions are assumed to be accurate within few percent.

The resonance properties (f_0, Q) are obtained from fits to the measured responses, such as shown in Fig. 4.1. Note the large difference in the resonance frequency f_0, when comparing the results in liquid ^{4}He and vacuum. The difference is explained by the hydrodynamic added mass from motion of the liquid by the res-

Table 4.1: Dimensions and measured properties of the MEMS devices studied in this work. Some of the properties were not measured for all the devices and the corresponding fields are left empty.

Device	5NF	5NN	5NV
L (µm)	14.7	22.0	28.9
H (µm)	13.0	13.2	13.2
w (µm)	1.11	1.10	1.10
d (nm)	150	150	150
$f_{0,\mathrm{vac}}$ (kHz)	395.2	335.6	291.8
$f_{0,\mathrm{LHe}}$ (kHz)	337.8	288.9	251.1
Q (16 mK, 83 mT)	20300	21400	19000
Q (16 mK, 27 mT)	35500		33600
N $(T < T^*)$	0.43 ± 0.10	0.54 ± 0.40	0.48 ± 0.10
N $(T > T^*)$	0.04 ± 0.02		0.08 ± 0.03
β_{vac} (Hz/nm^2)	-0.081		-0.020
β_{LHe} (Hz/nm^2)	-0.25	-0.041	-0.098

onator, as explained in section 2.4. The relative change in the resonance frequencies ($f_{0,\mathrm{LHe}}/f_{0,\mathrm{vac}} \approx 86\%$) agree with the result of Eq. (2.40) within 1.5%, when the tabulated values for the dimensions (w, d) and the known densities of the superfluid (150 kg/m^3) and Al (2700 kg/m^3) are used.

The Q-values presented in the table were measured in vacuum at $T = 16$ mK, with Al in the normal state ($B = 83$ mT) and in the superconducting state ($B = 27$ mT). At a first glance it might seem that the Q-value increases in the superconducting state. However, the apparent increase in Q is likely due to the smaller magnetomotive

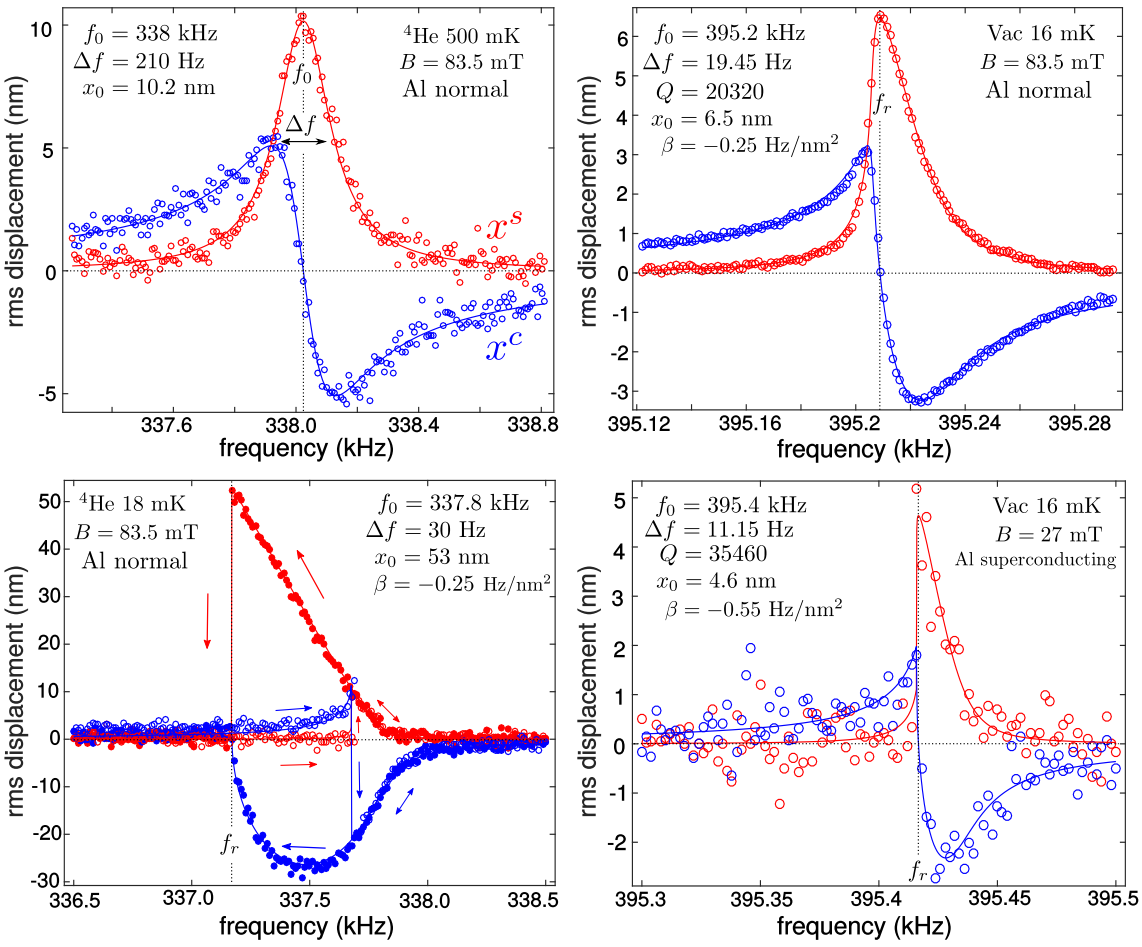

Figure 4.1: Four resonance responses of the sample 5NF. The red and blue circles represent the measured displacement out-of-phase x^s and in-phase x^c with the driving force, respectively. The solid lines are fits. (top left): A linear resonance response, measured in liquid ^{4}He at T=500 mK. (top right): A slightly nonlinear response measured in vacuum at T=16 mK. (bottom left): A nonlinear response measured in liquid ^{4}He at T=18 mK. The filled circles correspond to sweep in the decreasing frequency direction, while the empty circles correspond to sweep in the increasing frequency direction. The sweep directions are indicated with the arrows as well. (bottom right): A nonlinear response measured in the decreasing frequency direction in vacuum at T=16 mK with the aluminium in the superconducting state.

damping in the smaller magnetic field, as discussed in section 4.1. Although the superconducting transition seems to have a minute influence on the damping, it does have a measurable effect on the resonance frequency. Typically, a positive shift ($\sim$ 200 Hz) in the resonance frequency is observed at the transition from the normal state to the superconducting state (see the top right and bottom right panels of Fig. 4.1 for an example). The frequency shift can be attributed to an extra spring constant which arises when the magnetic field is expelled from the superconductor.

The values of N presented in the table are obtained from fits to the measured temperature dependences of the intrinsic damping ($\propto T^N$), as discussed in section 4.1. The observed values $N(T < T^*)$ match closely the value $N = 0.5$ expected for 1D phonon mediated TLS losses in flexural resonators (section 2.3.3).

Examples of measured resonance responses of the sample 5NF can be seen in Fig. 4.1. The response is linear when the amplitude of oscillations is small compared to the threshold value $x_0 \ll x_c$ and fits to the equations (2.9) and (2.10) present the data well (see Fig. 4.1, top left panel). Nonlinear effects become apparent near the threshold oscillation amplitude $x_0 \lesssim x_c$. The resonance response is then fit to the nonlinear equations (2.16) and (2.17) (see Fig. 4.1, top right panel). At even larger amplitudes $x_0 > x_c$, the solutions become multivalued and hysteresis depending on sweep direction appears (see Fig. 4.1, lower left panel). When sweeping in the decreasing frequency direction, the out-of-phase component of the displacement x_1^s is practically triangular and the in-phase component x_1^c is semi-circular, and the resonance frequency f_r is shifted quadratically with the oscillation amplitude. When sweeping in the increasing frequency direction, the amplitude of the peak is significantly smaller. The observed behaviour is in agreement with the theory presented in section 2.2.3. The values of β shown in Table 4.1 are obtained by measuring the shift of the nonlinear resonance frequency with increasing oscillation amplitude, as discussed in section 4.2. Note how the devices become more nonlinear in the superfluid with $\beta_{\mathrm{LHe}} < \beta_{\mathrm{vac}}$.

With the spring constant $k_{5\mathrm{NF}} \approx 0.060\,\mathrm{N/m}$ of the device 5NF, resolution on the quality factor $\Delta Q/Q \approx 0.1$, maximum displacement $x_{\max} \approx 5\,\mathrm{nm}$ and $Q \approx 3.5 \times 10^4$ (4.1, bottom right panel), the force resolution given by Eq. (2.7) is $|F_d| \approx 1\,\mathrm{fN}$. The resolution on the (linear) resonance frequency is somewhat limited by the nonlinearity at lowest temperatures, but the approximation $\Delta f_0 \approx \frac{1}{2}\Delta f$ (see section 2.2.1) seems reasonable. Similar figures are expected for the other devices. Thus, the devices are capable of detecting dissipative (and inertial) forces which correspond to a small fraction (0.001) of the tension of a vortex line ($\sim 1\,\mathrm{pN}$) in superfluid ^{4}He. Measurements on the dynamics of a single quantum vortex are feasible with such devices.

4.1 Damping

The temperature dependence of the line width Δf for the sample 5NF, measured in vacuum and superfluid ^{4}He at 3 bar pressure is shown in Fig. 4.2. At low temperatures, the damping is weak and the sweeps are nonlinear even with the weakest driving forces. The damping coefficient $\gamma = 2\pi\Delta f$ is then obtained from fits to the nonlinear Eqs. (2.16) and (2.17), and the corresponding effectively linear Δf is presented. At higher temperatures the line width increases and the response becomes practically linear. In this case, the width is obtained from fits to the Eqs. (2.9) and (2.10).

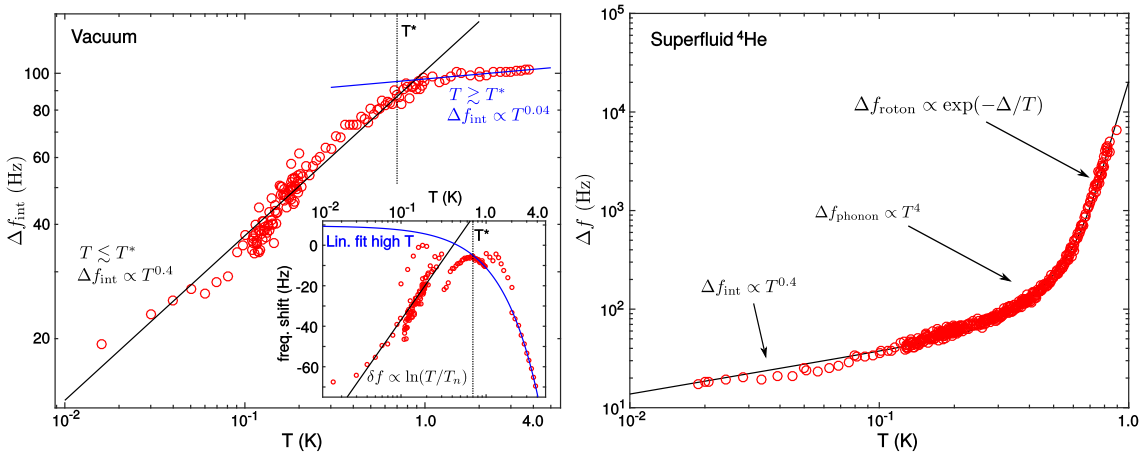

Figure 4.2: (left:) Resonance line width $\Delta f_{\rm int} = \gamma/(2\pi)$ (main panel) and frequency shift (inset) as a function of temperature, measured in vacuum for sample 5NF. The zero of the frequency shift corresponds to the highest measured resonance frequency. The dashed lines indicate the maximum of the frequency shift, which corresponds to the crossover temperature T^*. The solid lines are fits. (right:) Resonance line width as a function of temperatuere measured in superfluid ^{4}He. The solid line is a fit to the data, with contributions from the intrinsic losses and ballistic drag due to phonons and rotons. The relative weight of the different damping mechanisms change as a function of temperature, and the arrows indicate where each contribution is most relevant.

4.1.1 Intrinsic width

The intrinsic (vacuum) width depends on the temperature as $\Delta f_{\rm int} = a_{\rm int} T^N$. The dependence has two distinct temperature regimes with a cross-over temperature around $T^* \approx 0.7\,$K. At $T < T^*$, the damping has a relatively steep temperature dependence, and the resonance frequency increases logarithmically with temperature. Saturation of the width to a constant value at the lowest temperatures is not observed, and higher Q-values can possibly be obtained at even lower temperatures. At $T > T^*$ the temperature dependence of damping is rather weak, and the resonance

frequency decreases linearly. The cross-over temperature is taken as the position of the maximum of the resonance frequency, as shown in the inset of Fig. 4.2.

The exponents N in Table 4.1 are obtained from fits to the measured line widths at the different temperature regimes, as shown in Fig. 4.2 (left panel). The relative error between the measured vacuum width and the power law fit for sample 5NF can be seen in Fig. 4.3. There is a clear pattern in the error, which indicates that the power-law model used to fit the data has some limitations. The obtained values for N depend somewhat on the chosen temperature range, which is taken into account in the given error estimates. The scatter of the error around the mean in Fig. 4.3 is due to the errors in the measured width and temperature. The higher error at lowest temperatures is due to the smaller amplitudes of the signals combined with the nonlinearity of the sweeps. The temperature dependence of the intrinsic width has not been measured in vacuum for the device 5NN, but it is determined from the temperature depencence of the measured width in superfluid ^{4}He at the lowest temperatures $T < 200\,\mathrm{mK}$, where the contribution from the liquid to the width is almost negligible. Due to the small temperature range, limited amount of data and small contribution from the liquid, the corresponding error estimate (based on 95% confidence bounds of the fit) is very large, and the value obtained for the device 5NN is only indicative.

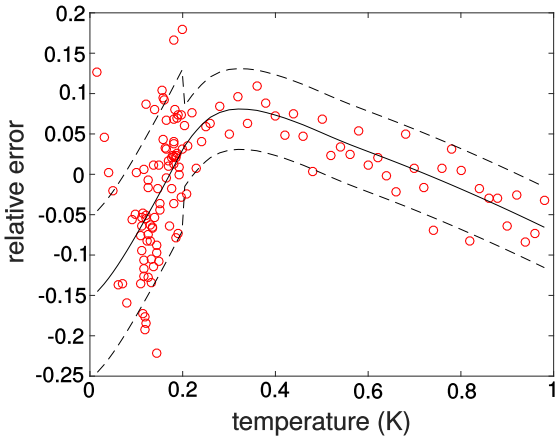

Figure 4.3: The relative error between the measured vacuum width and the power law fit for sample 5NF. The solid line is a moving average of the error and most of the data fall between the dashed lines, which are 10% apart from the mean at $T < 0.2\,\mathrm{K}$ and 5% apart from the mean at $T > 0.2\,\mathrm{K}$.

The observed temperature dependence in vacuum is attributed to tunneling two level systems present in the device, as discussed in section 2.3.3. The exponent N measured at low temperature is close to the value $N = 0.5$ predicted for 1D-phonons coupling to the TLSs in flexural resonators. Assuming a density of states $P_0 = 10^{44}\mathrm{J}^{-1}\mathrm{m}^{-3}$, and a 5% fraction of amorphous metal in the structure, a fit to Eq. (2.38) gives a reasonable phonon-TLS coupling constant $\gamma_e \approx 2.1\,\mathrm{eV}$. The observed frequency shift (logarithmic at low T and linear at high T) is characteristic to TLSs in metallic glasses, although the maximum in frequency is observed at

a rather low temperature $T^* \approx 0.7\,\mathrm{K}$ (typically $2\,\mathrm{K} \gtrsim T^* \gtrsim 3\,\mathrm{K}$ in bulk metallic glasses). The aforementioned values of P_0 and γ_e together with the elastic modulus $E = 70\,\mathrm{GPa}$ also produce quantitatively and qualitatively the observed frequency shift $\delta f_0/f_0 = 0.8 \times 10^{-4} \ln(T/T_n)$, when they are inserted in Eq. (2.37). This perfect agreement should be treated with caution, since we did not consider the fraction of amorphous metal in the expression for the frequency shift, Eq. (2.37), which is typically attributed to fully amorphous metals. Note that the expression for amorphous insulators, Eq. (2.35), also produces the logarithmic temperature dependence at $T < T^*$, although the logarithmic decrease in frequency, Eq. (2.36) expected at $T > T^*$, is not observed.

Magnetomotive damping

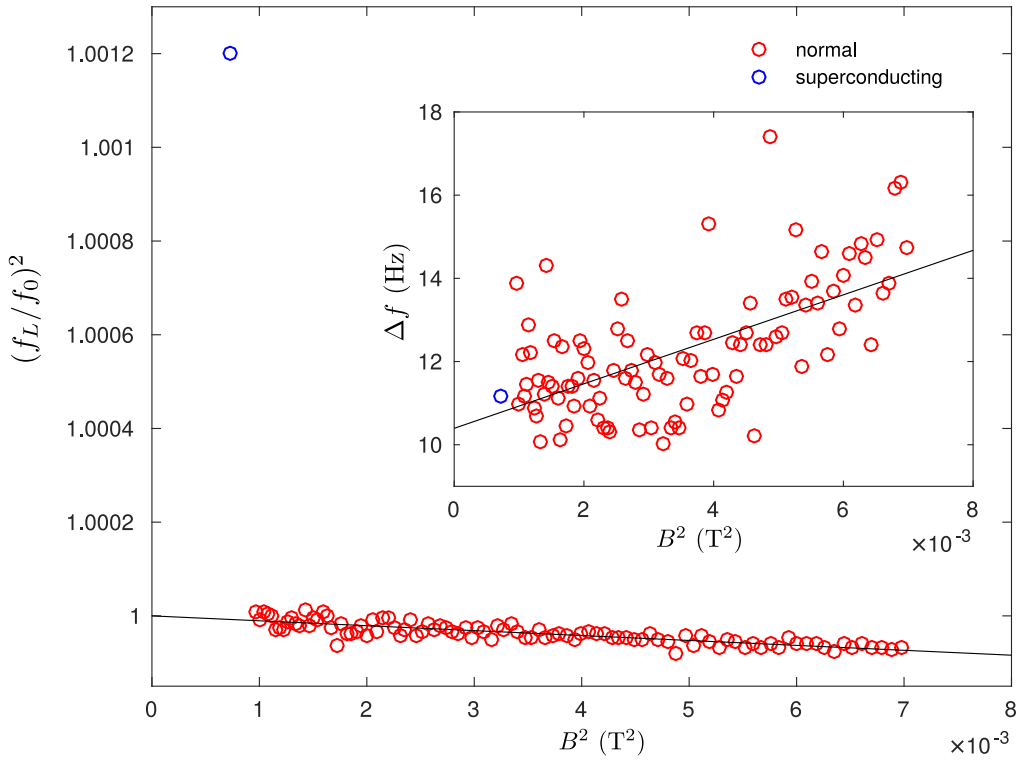

Figure 4.4: Magnetic field dependence of the resonance frequency f_0 (main panel) and line width $\Delta f\gamma/2\pi$ (inset) for device 5NF, measured in vacuum at $T = 16\,\mathrm{mK}$. The solid lines are fits to Eqs. (2.23) and (2.24).

We have measured the magnetic field dependence of damping and resonance frequency at $T = 16\,\mathrm{mK}$ in vacuum for sample 5NF and the results are presented in Fig. 4.4. From theory (section 2.3.1), we would have expected the effect of magnetomotive damping to be negligible. However, the measured properties show the B^2 dependence in both width and resonance frequency, as expected for magnetomotive damping. The effect is usually assumed to be temperature independent.

However, the sweeps at this low temperature are slightly nonlinear, which might contribute to the observed behaviour. The contribution to the width in vacuum at the lowest temperature and at the maximum magnetic field is approximately 30%. In superfluid ^{4}He, the contribution to the total width is obviously smaller. So far the magnetomotive damping has been treated as an additional source of error in the determined exponent N for the TLS losses, but in future a more accurate analysis can be done.

Note how the transition to the superconducting state has a considerable effect on the resonance frequency, but the effect to the line width is within the scatter of measurements. The result implies that electrons do not contribute essentially to the dissipation mechanism in our devices, contradictory to the result in [37], where they find different exponent N in the superconducting and normal states. The main difference in our and their devices is the absence of a silicon layer in ours. As stated in [37], the stress at the Si-Al interface may contribute to the change of N at the superconducting transition in their devices.

The magnetomotive damping effect may also be used to control damping, if the magnetic field is strong enough. This might become beneficial at the lowest temperatures, where the nonlinearity often causes trouble. The cost of increasing the magnetic field is of course a lower Q-value and the corresponding loss in force sensitivity. However, the loss is compensated by a higher signal-to-noise ratio and more linear response, since the threshold amplitude for nonlinearity depends on the damping. There is then some optimal magnetic field value, for which the highest force resolution is obtained.

4.1.2 Thermometry in superfluid ^{4}He

In superfluid ^{4}He, the resonance line width increases further due to the ballistic phonon $\Delta f_{\mathrm{phonon}} \propto T^4$ and roton drag $\Delta f_{\mathrm{roton}} \propto \exp(-\Delta_{\mathrm{rot}}/T)$, according to Eqs. (2.45) and (2.46). The measured width Δf is a sum of the different contributions $\Delta f = \Delta f_{\mathrm{int}} + \Delta f_{\mathrm{phonon}} + \Delta f_{\mathrm{roton}}$. To fit the data, the vacuum contribution is first subtracted from the data, so that only phonon and roton contributions remain. The roton contribution to the width falls exponentially with decreasing temperature, and becomes negligible below $T = 0.5\,\mathrm{K}$, where the contribution to the total width is already less than 1.5%. The phonon contribution is then obtained from a fit to the data below $T < 0.5\,\mathrm{K}$ as shown in Fig. 4.5 (left panel). The fit gives $\Delta f_{\mathrm{phonon}} = 2200\,\mathrm{HzK}^{-4}T^4$, which is approximately two times the value predicted by Eq. (2.45). When the intrinsic width and the fitted phonon contribution to the width are removed from the total width, we are left with the roton drag, shown in the right panel of Fig. 4.5. The fit to the data gives $7.6 \times 10^7\,\mathrm{Hz}\exp(-\Delta_{\mathrm{rot}}/T)$, which corresponds to approximately 40% of the value predicted from Eq. (2.46).

The temperature dependent intrinsic width and ballistic drag enable thermometry with the MEMS devices in vacuum and superfluid ^{4}He down to milliKelvin temper-

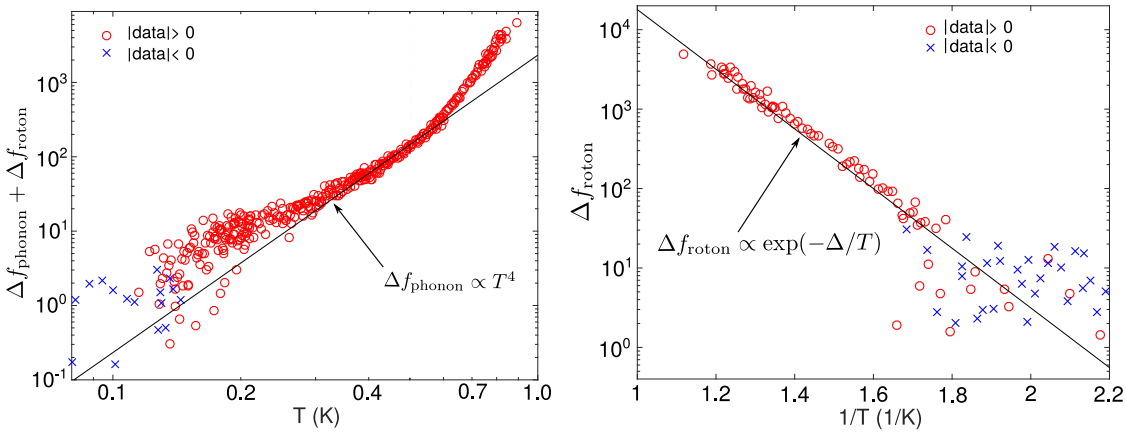

Figure 4.5: (left): Width due to the ballistic phonon and roton drag in superfluid ^{4}He (red circles) and fit to the phonon drag (solid line) below $T = 500\,\mathrm{mK}$. The effect of rotons to the drag becomes visible above $T = 600\,\mathrm{mK}$. Below $T = 300\,\mathrm{mK}$ the width due to ballistic drag becomes small compared to the intrinsic width ($\Delta f_{\mathrm{phonon}} < 0.3\Delta f_{\mathrm{int}}$) and deviations from the fit arise due to limitations of the model used for the intrinsic width. At the lowest temperatures the errors (in negative direction) become larger than the width due to ballistic drag and negative data arise. To present all the data in a single logarithmic plot, the negative data (blue crosses) are mirrored to the positive axis. (right): Width due to the roton drag (red circles) and fit (solid line) to Eq.(2.46). As in the figure on the left, the negative data is mirrored to the positive side and shown with the blue crosses.

atures. The relative error in the temperature is given by the expression

$$\left|\frac{\Delta T}{T}\right| = \frac{1}{\alpha_{\mathrm{res}}}\left|\frac{\Delta(\Delta f)}{\Delta f}\right|, \tag{4.1}$$

where the factor α_{res} depends on the dominant loss mechanism, and $|\Delta(\Delta f)/\Delta f|$ is the relative error in the measured width. The intrinsic width is the only loss mechanism in vacuum and dominates in superfluid ^{4}He below 300 mK. For the intrinsic width $\alpha_{\mathrm{res}} = N$. Phonon drag is important from 300 mK to 700 mK, where $\alpha_{\mathrm{res}} = 4$. The roton drag dominates at $T > 700\,\mathrm{mK}$, where $\alpha_{\mathrm{res}} = \Delta/T$. The relative error between the measured width and the fits at different temperatures are shown in Fig. 4.6. For most accurate measurements of temperature, the systematic error (the observed pattern in the error) should be compensated, leaving only the scatter, which is always smaller than 10%. This would result in a relative error $|\Delta T/T| = 23\%$, when measured in vacuum below $T = 1\,\mathrm{K}$. The same accuracy is expected in superfluid ^{4}He below 300 mK, while relative error of 2.5% is expected from 300 mK to 700 mK and 1% above 700 mK.

In the absence of resonant amplification, acoustic emission in the liquid ^{4}He would show as a temperature independent contribution to the width. Such effect is not seen in the relative error shown in Fig. 4.6. The pattern in the error at low temperatures, where intrinsic width dominates, is similar to the pattern in error observed in vacuum.

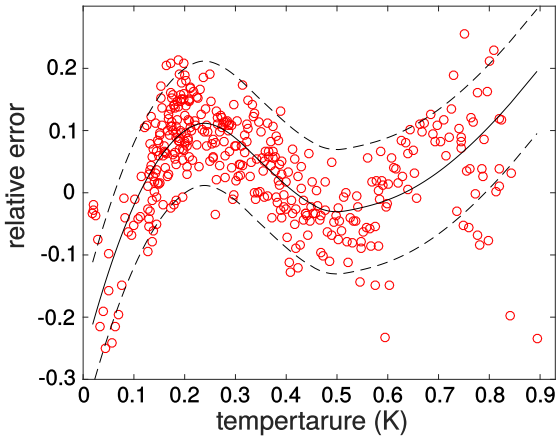

Figure 4.6: The relative error between the measured width in superfluid ^{4}He and the full fit. The solid line is a sliding average of the error. Most of the data fall between the dashed lines, which are 10% apart from the average error.

The increased error at high temperature may be attributed to the slight decrease in the value of the roton gap Δ_{rot} with increasing temperature.

4.2 Nonlinear frequency shift

In vacuum, at moderate excitation currents and in 83 mT magnetic field (normal state), the value of β is temperature independent (at $T < 2$ K). The shift of the resonance frequency follows the expected quadratic dependence on amplitude as shown in Fig. 4.7. However, in superfluid ^{4}He, the devices become more nonlinear with $\beta_{LHe} < \beta_{vac}$. The decrease of β has been observed also in ^{3}He by Defoort et al. in [10], where they use goal-post shaped MEMS devices. The behaviour may be attributed to a nonlinear increase in effective mass in the superfluids.

We find a negative β for all the devices, which is in a qualitative agreement with the FEM simulations presented in section 2.2.4. However, the magnitude obtained from the simulations $|\beta| \sim 1 \times 10^{-3}\,\mathrm{Hz/nm^2}$ is smaller than the measured value $|\beta| \sim 0.1\,\mathrm{Hz/nm^2}$ by two orders of magnitude. A possible explanation for the large disagreement between simulations and experiment is the static stress and stain in the structures (section 3.1), which have been neglected in the simulations.

It seems that the value of β depends somewhat on the excitation current and magnetic field. At very low current and field, the magnitude $|\beta|$ is enhanced, while at moderate drive/field it becomes constant. For example, the $|\beta| = 0.25\,\mathrm{Hz/nm^2}$ measured in vacuum at $T = 16$ mK with small excitation current and in a typical magnetic field $B = 83$ mT (Fig. 4.1, top right panel) is three times as large as the constant value observed in vacuum at higher excitation currents $|\beta| = 0.081\,\mathrm{Hz/nm^2}$. In the superconducting state, the nonlinearity seems to become even stronger. For example, the $|\beta| = 0.55\,\mathrm{Hz/nm^2}$ (see Fig. 4.1, bottom right panel) measured at the

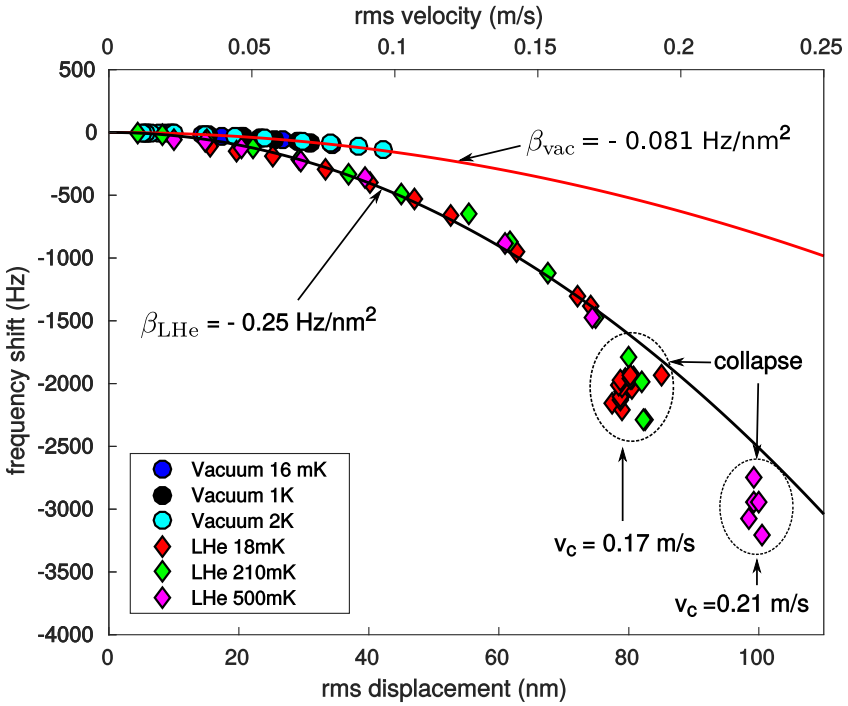

Figure 4.7: Nonlinear frequency shift at resonance, measured for sample 5NF in vacuum (circles) and He-II (diamonds) at various temperatures with Al in normal state ($B = 83\,\mathrm{mT}$). The duffing parameter β is obtained from the quadratic fits (solid lines).

same 16 mK temperature in the superconducting state is approximately two times as large as the result in the normal state with low excitation current (4.1, top right panel). Note that the oscillation amplitude in the superconducting state is somewhat smaller than in the normal state. It is difficult to tell if the difference in β is due to the superconductivity or the amplitude difference in this case. The enhancement of $|\beta|$ at low currents and fields is not well understood, but similar behaviour has been reported for goal-post shaped MEMS devices in the supplementary material of [37]. Since the intrinsic damping of the devices is dominated by tunneling two level systems (section 4.1), one may consider if the dissipation mechanism plays some role in the nonlinear frequency shift. Indeed, the resonant TLS damping mechanism is known to cause nonlinear dissipation, when it is not yet saturated [33, 43] (at very small elastic fields) and could in principle also cause a nonlinear frequency shift (through Kramers-Kronig relations). The resonant TLS damping mechanism is supposed to be saturated already at very small oscillation amplitudes ($\gtrsim$ 1Å), and should only contribute to a linear frequency shift, as discussed in section 2.3.3. However, since the observed change in the value of β occurs at the smallest amplitudes, one might speculate that the resonant TLSs are not saturated. The apparent dependence of $|\beta|$ on the magnetic field is somewhat difficult to understand in this picture, but it does point towards interesting study directions. Perhaps the change is related to the superconducting state which gives rise to an additional (nonlinear)

spring constant, maybe the TLSs and the magnetic field interact in some way, or the effect is simply amplitude-dependent. To study the effect, systematic measurements on many combinations of excitation currents, magnetic fields and oscillation amplitudes are required. Unfortunately, these low-amplitude measurements are rather time-consuming, since the signals are small and require quite a lot of signal averaging. The few data points we have obtained from measurements at low amplitudes give only a qualitative description (increase in $|\beta|$) and more measurements would be required to fully characterize the phenomenon.

Also at the highest oscillation amplitudes in superfluid ^{4}He, a deviation from the expected quadratic frequency shift occurs (Fig. 4.7). The deviation is due to a collapse of oscillations before the resonance condition is reached. We attribute the collapse to emission of vortex rings, which is discussed further in section 4.3. The critical velocity v_c for the collapse increases with increasing temperature. The average velocities of the collapses at the three different temperatures are $v_c(18\,\mathrm{mK}) = 0.168\,\mathrm{m/s}$, $v_c(210\,\mathrm{mK}) = 0.172\,\mathrm{m/s}$ and $v_c(500\,\mathrm{mK}) = 0.21\,\mathrm{m/s}$.

4.3 Emission of vortex rings

We discuss here briefly a peculiar feature observed in superfluid ^{4}He at large oscillation amplitudes. When the excitation force is increased, and the velocity reaches a critical value $v_c = 0.17\,\mathrm{m\,s^{-1}}$ (at $T = 18\,\mathrm{mK}$), we observe a collapse of oscillations independently of the driving force, as shown in Fig. 4.8. The collapse differs from the jump phenomenon, which is characteristic to the Duffing oscillator. At resonance, the velocity should be exactly in phase with the excitation force and the dispersion component should go to zero continuously when approaching resonance, as seen from Eqs. (2.16) and (2.17). This behaviour is indeed observed at moderate drives, where the out-of-phase velocity (dispersion) component is practically semi-circular and the maximum of the triangular in-phase velocity (absorption) component increases with the driving force as expected. The collapse of oscillations at high driving forces is observed as a discontinuous jump in the dispersion component, which becomes larger with increasing driving force. Also, the maximum of the absorption component decreases with increasing drive, which is not expected behaviour.

The observed critical velocity is in reasonable agreement with the expected value for quantum turbulence mediated by the excitation of Kelvin waves, and the peak velocity $\sqrt{2}v_c$ corresponds to a prefactor $A' = 0.56$ in Eq. (2.48). If resonant amplification is allowed, the onset may happen at a lower velocity. One possible explanation for the collapse is a sudden increase of the drag force, when a vortex ring is emitted. As discussed in section 2.4, the emission of a vortex ring which carries momentum with it gives a kick to the device. This kick may be strong enough to cause a transition to the other stable branch and premature collapse of oscillations. Supporting this explanation is the fact that the wavelength of Kelvin waves at the device frequency matches the beam width and that the self induced velocity of such

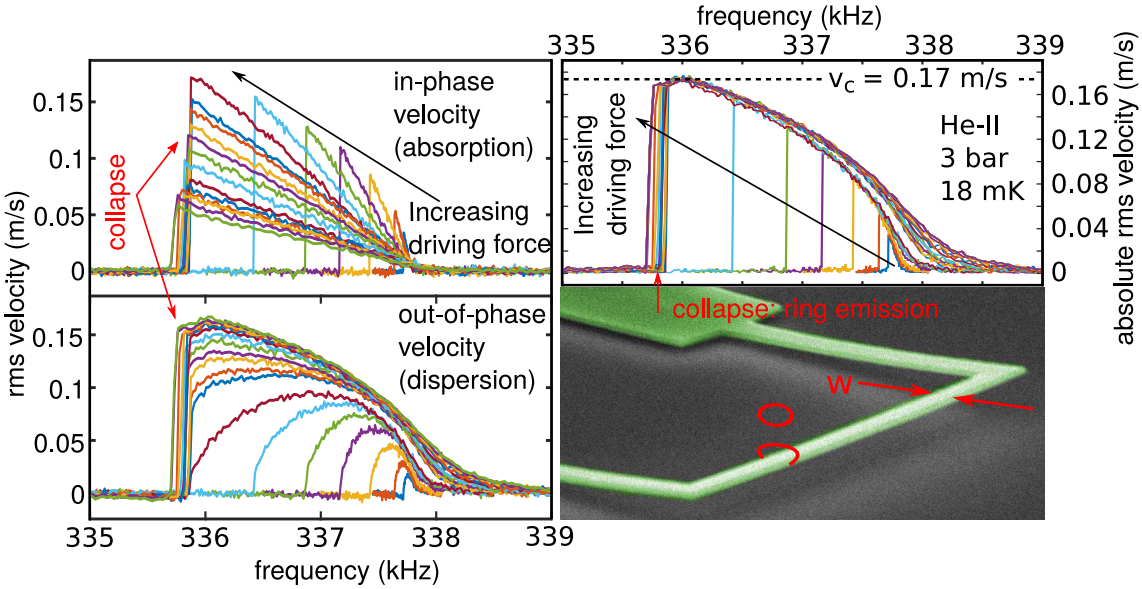

Figure 4.8: (left:) The in-phase (top) and out-of-phase (bottom) components of the velocity of the beam measured in He-II at $T = 18\,\mathrm{mK}$ in the decreasing frequency direction at different driving forces. Each line presents a frequency sweep conducted at one driving force, and the colour coding in all the line plots in this figure is the same. (right top): The absolute velocity of oscillations show that the collapse occurs always after reaching velocity $v_c = 0.17\,\mathrm{m\,s^{-1}}$ independently of the driving force. The colour coding of the lines is the same as in the figures on the left. (right bottom:) A schematic figure of emission of a vortex ring from the structure.

a vortex ring is close to the observed critical velocity. A vortex attached to the beam could possibly have resonant amplification of a Kelvin wave, which could eventually lead to a self-reconnection and formation of the vortex ring. Note that the vortex ring does not necessarily have to form exactly as depicted in Fig. 4.8 (lower right panel). For example, a remnant vortex could be stretched between the other leg and the beam in the corner. One would imagine that resonant amplification of Kelvin waves is more easily mediated for such a configuration. At higher temperatures, the critical velocity is larger, as shown in Fig. 4.7. This may be explained by mutual friction, which damps the growth of Kelvin waves.

Chapter 5

Conclusions

In conclusion, the response of magnetomotively driven suspended aluminium MEMS resonators have been measured at low temperatures in vacuum (16 mK – 4 K) and superfluid ^{4}He (18 mK – 1 K). The force resolution $\Delta f \sim 1$ fN of the devices is expected to be sufficient for studying dynamics of a single vortex pinned to the device.

The damping of the devices in vacuum at $T < 1$ K depend on temperature as T^N with $N = 0.43$-0.54 and the resonance frequency increases logarithmically with temperature. The behaviour is attributed to tunneling two level systems in the devices. A model considering TLSs in the naturally formed aluminium oxide layer and 1D phonon mediated relaxation of the TLSs predicts an exponent $N = 0.5$, which is close to the observed values. Quantitative predictions of the model are successful in providing the correct magnitude of the Q-value with reasonable assumptions on parameters. Superconducting transition does not affect the observed damping within the measurement accuracy. However, the damping depends on the magnetic field due to the external magnetomotive damping mechanism.

In superfluid ^{4}He the damping increases further due to ballistic phonon and roton drag. Damping due to acoustic emission is not observed. The temperature dependent intrinsic width and ballistic drag enable thermometry with these devices at the milliKelvin temperature range. The MEMS devices are sensitive to temperature (with approximately 20% accuracy) down to ~ 10 mK temperature in superfluid ^{4}He, whereas the macroscopic counterparts (vibrating wires and tuning forks) typically become insensitive to temperature below 100 mK.

At large oscillation amplitudes, the devices show nonlinear Duffing-like behaviour, where the resonance frequency is shifted towards lower frequencies quadratically with an increasing oscillation amplitude. The resonance properties are then obtained from fits to modified Lorentzian functions, which account for the nonlinearity. The sign of the frequency shift is reproduced in simulations. The stress and strain in the fabricated structures is thought to be the source of the larger nonlinearity in the real-world samples compared to simulations. The nonlinear frequency shift is found

to be larger in superfluid ^{4}He, which can be qualitatively explained by a nonlinear increase in the effective mass. At small excitation currents and magnetic fields, the magnitude of β increases. The effect is rather poorly understood, but the effect of resonant TLS dissipation mechanism has been considered as a possible source for this behaviour. The understanding of the nonlinear properties are important from a practical as well as a theoretical point of view, and the low amplitude properties deserve to be studied further.

Capabilities of such devices to detect single-vortex processes are demonstrated by the observed collapse of oscillations at large oscillation amplitudes in ^{4}He. We interpret the collapse as a sudden increase of the effective drag force, when the critical velocity for emission of a vortex ring is exceeded.

Scaling of these devices to the nanoscale is relatively easy, and will be considered. Given that the force resolution of these devices should be sufficient, we plan to fabricate new resonators with a trapping site for a vortex, which will be pinned between the resonator and another trapping site on the substrate. The sample will then be installed in a rotating cryostat, where creation and destruction of vortices is well controlled, especially in ^{3}He. We will then be able to measure the dynamic forces that the vortex line exerts on the device. Comparison between ^{3}He and ^{4}He is especially interesting since the vortex core structures in the two superfluids are very different. Core-bound fermion states in ^{3}He are expected to contribute essentially to vortex dynamics. Additionally, we will collect valuable new information on nonlinearity and damping of metallic micro- and nanoscale resonators, which are limited by tunneling TLSs.

Bibliography

[1] E. Kozik and B. Svistunov. Kelvin-wave cascade and decay of superfluid turbulence. *Phys. Rev. Lett.* **92**, 035301 (2004).

[2] M. Blažková, M. Človečko, V. B. Eltsov, E. Gažo, R. de Graaf, J. J. Hosio, M. Krusius, D. Schmoranzer, W. Schoepe, L. Skrbek, P. Skyba, R. E. Solntsev, and W. F. Vinen. Vibrating quartz fork–a tool for cryogenic helium research. *Journal of Low Temperature Physics* **150**, 525 (2008).

[3] R. Blaauwgeers, M. Blazkova, M. Človečko, V. B. Eltsov, R. de Graaf, J. Hosio, M. Krusius, D. Schmoranzer, W. Schoepe, L. Skrbek, P. Skyba, R. E. Solntsev, and D. E. Zmeev. Quartz tuning fork: Thermometer, pressure- and viscometer for helium liquids. *Journal of Low Temperature Physics* **146**, 537 (2007).

[4] E. Pentti, J. Rysti, A. Salmela, A. Sebedash, and J. Tuoriniemi. Studies on helium liquids by vibrating wires and quartz tuning forks. *Journal of Low Temperature Physics* **165**, 132 (2011).

[5] A. Salmela, J. Tuoriniemi, and J. Rysti. Acoustic resonances in helium fluids excited by quartz tuning forks. *Journal of Low Temperature Physics* **162**, 678 (2011).

[6] A. Kraus, A. Erbe, and R. H. Blick. Nanomechanical vibrating wire resonator for phonon spectroscopy in liquid helium. *Nanotechnology* **11**, 165 (2000).

[7] E. Collin, L. Filleau, T. Fournier, Y. M. Bunkov, and H. Godfrin. Silicon vibrating wires at low temperatures. *Journal of Low Temperature Physics* **150**, 739 (2008).

[8] M. Gonzalez, P. Zheng, B. H. Moon, E. Garcell, Y. Lee, and H. B. Chan. Unusual behavior of a MEMS resonator in superfluid 4He. *Journal of Low Temperature Physics* **171**, 200 (2013).

[9] G. I. Harris, D. L. McAuslan, E. Sheridan, Y. Sachkou, C. Baker, and W. P. Bowen. Laser cooling and control of excitations in superfluid helium. *Nature Physics* **12**, 788 (2016).

[10] M. Defoort, S. Dufresnes, S. L. Ahlstrom, D. I. Bradley, R. P. Haley, A. M. Guénault, E. A. Guise, G. R. Pickett, M. Poole, A. J. Woods, V. Tsepelin,

S. N. Fisher, H. Godfrin, and E. Collin. *Journal of Low Temperature Physics* **183**, 284 (2016).

[11] D. I. Bradley, R. George, A. M. Guénault, R. P. Haley, S. Kafanov, M. T. Noble, Yu. A. Pashkin, G. R. Pickett, M. Poole, J. R. Prance, M. Sarsby, R. Schanen, V. Tsepelin, T. Wilcox, and D. E. Zmeev. Operating nanobeams in a quantum fluid. *Scientific Reports* **7**, 4876 (2017).

[12] T. Kamppinen. Aluminium microelectromechanical resonator for studying cryogenic fluids. Special assignment (2017).

[13] E. Oberg, F. Jones, H. Horton, H. Ryffel, and C. McCauley. *Machinery's Handbook*. Industrial Press, 30th edition, (2016).

[14] M. A. Haque and M. T. A. Saif. Deformation mechanisms in free-standing nanoscale thin films: A quantitative in situ transmission electron microscope study. *Proc Natl Acad Sci U S A* **101**, 6335 (2004).

[15] E. Collin, Yu. M. Bunkov, and H. Godfrin. Addressing geometric nonlinearities with cantilever microelectromechanical systems: Beyond the Duffing model. *Physical Review B* **82**, 235416 (2010).

[16] S. Joshi, S. Hung, and S. Vengallatore. Design strategies for controlling damping in micromechanical and nanomechanical resonators. *EPJ Techniques and Instrumentation* **1**, 5 (2014).

[17] A. N. Cleland and M. L. Roukes. External control of dissipation in a nanometer-scale radiofrequency mechanical resonator. *Sensors and Actuators A: Physical* **72**, 256 (1999).

[18] M. C. Cross and R. Lifshitz. Elastic wave transmission at an abrupt junction in a thin plate with application to heat transport and vibrations in mesoscopic systems. *Physical Review B* **64**, 085324 (2001).

[19] D. M. Photiadis and J. A. Judge. Attachment losses of high Q oscillators. *Applied Physics Letters* **85**, 482 (2004).

[20] N. E. Phillips. Heat capacity of aluminum between 0.1 K and 4.0 K. *Physical Review* **114**, 676 (1959).

[21] A. L. Woodcraft. Recommended values for the thermal conductivity of aluminium of different purities in the cryogenic to room temperature range, and a comparison with copper. *Cryogenics* **45**, 626 (2005).

[22] J. Garai. Correlation between thermal expansion and heat capacity. *Computer Coupling of Phase Diagrams and Thermochemistry* **30**, 354 (2006).

[23] K. O. McLean. Low temperature thermal expansion of copper, silver, gold and aluminum. *Retrospective Theses and Dissertations*, page 4127 (1969).

[24] R. Griessen and H. R. Ott. The volume change between normal and superconducting aluminium above 0.3 K. *Physics Letters A* **36**, 113 (1971).

[25] C. Zener. *Elasticity and anelasticity of metals.* Univerity of Chicago Press, Chicago, Illinois, (1948).

[26] A. Akhiezer. On the absorption of sound in solids. *Journal of Physics (Moscow)* **1**, 277 (1939).

[27] W. B. Gauster. Low-temperature gruneisen parameters for silicon and aluminum. *Physical Review B* **4**, 1288 (1971).

[28] H. E. Bömmel and K. Dransfeld. Excitation and attenuation of hypersonic waves in quartz. *Physical Review* **117**, 1245 (1960).

[29] K. Kunal and N. R. Aluru. Akhiezer damping in nanostructures. *Physical Review B* **84**, 245450 (2011).

[30] M. L. Roukes, M. R. Freeman, R. S. Germain, R. C. Richardson, and M. B. Ketchen. Hot electrons and energy transport in metals at millikelvin temperatures. *Physical Review Letters* **55**, 422 (1985).

[31] J. Classen, T. Burkert, C. Enss, and S. Hunklinger. Anomalous frequency dependence of the internal friction of vitreous silica. *Physical Review Letter* **84**, 2176 (2000).

[32] A. D. Fefferman, R. O. Pohl, A. T. Zehnder, and J. M. Parpia. Acoustic properties of amorphous silica between 1 and 500 mK. *Physical Review Letters* **100**, 195501 (2008).

[33] W. A. Phillips. Two-level states in glasses. *Reports on Progress in Physics* **50**, 1657 (1987).

[34] C. Seoánez, F. Guinea, and A. H. Castro Neto. Surface dissipation in nanoelectromechanical systems: Unified description with the standard tunneling model and effects of metallic electrodes. *Physical Review B* **77**, 125107 (2008).

[35] G. Zolfagharkhani, A. Gaidarzhy, S.-B. Shim, R. L. Badzey, and P. Mohanty. Quantum friction in nanomechanical oscillators at millikelvin temperatures. *Physical Review B* **72**, 224101 (2005).

[36] A. Venkatesan, K. J. Lulla, M. J. Patton, A. D. Armour, C. J. Mellor, and J. R. Owers-Bradley. Dissipation due to tunneling two-level systems in gold nanomechanical resonators. *Physical Review B* **81**, 073410 (2010).

[37] K. J. Lulla, M. Defoort, C. Blanc, O. Bourgeois, and E. Collin. Evidence for the role of normal-state electrons in nanoelectromechanical damping mechanisms at very low temperatures. *Physical Review Letters* **110**, 177206 (2013).

[38] F. Hoehne, Yu. A. Pashkin, O. Astafiev, L. Faoro, L. B. Ioffe, Y. Nakamura, and J. S. Tsai. Damping in high-frequency metallic nanomechanical resonators. *Physical Review B* **81**, 184112 (2010).

[39] J. Sulkko, M. A. Sillanpää, P. Häkkinen, L. Lechner, M. Helle, A. Fefferman, J. Parpia, and P. J. Hakonen. Strong gate coupling of high-Q nanomechanical resonators. *Nano Letters* **10**, 4884 (2010).

[40] Seung B. S., June S. C., Seok W. K., Sung W. C., Sung W. C., Yun D. P., Pritiraj M., Nam K., and Jinhee K. Micromechanical resonators fabricated from lattice-matched and etch-selective GaAs InGaP GaAs heterostructures. *Applied Physics Letters* **91**, 133505 (2007).

[41] Y. Tao, J. M. Boss, B. A. Moores, and C. L. Degen. Single-crystal diamond nanomechanical resonators with quality factors exceeding one million. *Nature Communications* **5**, 3638 (2014).

[42] T. Faust, J. Rieger, M. J. Seitner, J. P. Kotthaus, and E. M. Weig. Signatures of two-level defects in the temperature-dependent damping of nanomechanical silicon nitride resonators. *Physical Review B* **89**, 100102 (2014).

[43] R. O. Behunin, F. Intravaia, and P. T. Rakich. Dimensional transformation of defect-induced noise, dissipation, and nonlinearity. *Physical Review B* **93**, 224110 (2016).

[44] J. Evertsson, F. Bertram, F. Zhang, L. Rullik, L.R. Merte, M. Shipilin, M. Soldemo, S. Ahmadi, N. Vinogradov, F. Carlà, J. Weissenrieder, M. Göthelid, J. Pan, A. Mikkelsen, J.-O. Nilsson, and E. Lundgren. The thickness of native oxides on aluminum alloys and single crystals. *Applied Surface Science* **349**, 826 (2015).

[45] A. J. Leggett and D. C. Vural. Tunneling two-level systems model of the low-temperature properties of glasses: Are smoking-gun tests possible? *The Journal of Physical Chemistry B* **117**, 12966 (2013).

[46] W. H. Chu. *Tech. Rep. No. 2, DTMB, Contract NObs-86396 (X) Southwest Research Institute; San Antonio, Texas, USA* (1963).

[47] L. Landau. Theory of the superfluidity of helium II. *Phys. Rev.* **60**, 356 (1941).

[48] D. G. Henshaw and A. D. B. Woods. Modes of atomic motions in liquid helium by inelastic scattering of neutrons. *Phys. Rev.* **121**, 1266 (1961).

[49] S. Balibar. Nucleation in quantum liquids. *Journal of Low Temperature Physics* **129**, 363 (2002).

[50] F. Caupin and S. Balibar. Cavitation pressure in liquid helium. *Phys. Rev. B* **64**, 064507 (2001).

[51] W. M. Whitney and C. E. Chase. Velocity of sound in liquid helium at low temperatures. *Physical Review Letters* **9**, 243 (1962).

[52] O. W. Dietrich, E. H. Graf, C. H. Huang, and L. Passell. Neutron scattering by rotons in liquid helium. *Phys. Rev. A* **5**, 1377 (1972).

[53] R.J. Donnelly. The landau parameters in helium II. *Physics Letters A* **39**, 221 (1972).

[54] J. S. Brooks and R. J. Donnelly. The calculated thermodynamic properties of superfluid helium 4. *Journal of Physical and Chemical Reference Data* **6**, 51 (1977).

[55] G. Baym, R. G. Barrera, and C. J. Pethick. Mobility of the electron bubble in superfluid helium. *Phys. Rev. Lett.* **22**, 20 (1969).

[56] J. Jäger, B. Schuderer, and W. Schoepe. Translational oscillations of a microsphere in superfluid helium. *Physica B: Condensed Matter* **210**, 201 (1995).

[57] W. F. Vinen and L. Skrbek. Quantum turbulence generated by oscillating structures. *Proceedings of the National Academy of Sciences* **111**, 4699 (2014).

[58] I. S. Sullivan, J. J. Niemela, R. E. Hershberger, D. Bolster, and R. J. Donnelly. Dynamics of thin vortex rings. *Journal of Fluid Mechanics* **609**, 319 (2008).

[59] D. Schmoranzer, M. La Mantia, G. Sheshin, I. Gritsenko, A. Zadorozhko, M. Rotter, and L. Skrbek. Acoustic emission by quartz tuning forks and other oscillating structures in cryogenic 4He fluids. *Journal of Low Temperature Physics* **163**, 317 (2011).

[60] *Bluefors LD Series*. Online, accessed 29.09.2017 `http://www.bluefors.com/index.php/ld-series`.

[61] *Ruthenium Oxide, Technical Specifications*. Online, accessed 29.09.2017 `https://www.lakeshore.com/products/cryogenic-temperature-sensors/ruthenium-oxide-rox-rtds/models/pages/Specifications.aspx`.